Bioactive Materials 50 (2025) 116–133

Contents lists available at ScienceDirect

Bioactive Materials

journal homepage: www.keaipublishing.com/en/journals/bioactive-materials

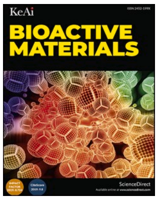

Elytra-inspired zirconium phosphate nanonetwork: Toward high-quality osseointegration and physical-chemical-mechanical bond at the interface for zirconia-based dental materials

Shuyi Wu [a,1], Yingyue Sun [a,1], Qihong Zhang [a], Wen Si [a], Peng Gao [a], Lei Lu [a], Zhennan Deng [a], Lihua Xu [b,*], Xinkun Shen [c,**], Jinsong Liu [a,***]

[a] *School and Hospital of Stomatology, Wenzhou Medical University, Wenzhou, 325027, China*
[b] *Department of General Medicine, First Affiliated Hospital, Wenzhou Medical University, Wenzhou, 325000, China*
[c] *Ningbo Key Laboratory of Skin Science, Ningbo College of Health Sciences, Ningbo, 315000, China*

ARTICLE INFO

Keywords:
Zirconia
Bionics
Self-assembly
Osseointegration
Bonding strength

ABSTRACT

Yttria-stabilized zirconia (YSZ) is widely used in dental implants and prostheses due to its excellent aesthetic and restorative properties. However, its bio-inert surface limits early osseointegration and weakens bonding strengths with porcelain veneer/resin cement. Inspired by the structure of beetle elytra, this work proposes a novel strategy involving a self-assembled trabecular-honeycomb biomimetic zirconium phosphate (ZrP) nanonetwork to modify YSZ surfaces. This approach simultaneously enhances energy dissipation, interfacial bonding, and osseointegration. The pore size of ZrP nanonetwork was precisely controlled by adjusting reaction temperatures (120 °C and 160 °C) and phosphoric acid concentrations (1.0 wt% and 2.5 wt%). Compared to conventional YSZ, the ZrP nanonetworks achieved remarkable improvements in bond strength, showing increases of 111 % with porcelain veneer and 336 % with resin cement. These enhancements are attributed to multiscale physical-chemical-mechanical interactions, including micromechanical anchoring, chemical bonding via phosphate groups, and energy dissipation through topological optimization. *In vitro* studies demonstrated that large-pore-size nanonetworks promote osteogenic differentiation of osteoblasts and modulate macrophage polarization toward the M2 phenotype, fostering an immune environment conducive to bone regeneration. *In vivo* experiments further validated the superior osseointegration and bone regeneration capacities of the large-pore-size ZrP nanonetwork. Collectively, this biomimetic ZrP nanonetwork-modified YSZ, with its exceptional physical-chemical-mechanical bonding properties, osseointegration potential, and immune-modulating capabilities, represents a groundbreaking advancement in zirconia-based material for dental implants and prostheses.

1. Introduction

Having satisfactory characteristics as a bio-ceramics inherent in the remarkable resistance to wear, fracture as well as corrosion, superior aesthetic properties, and favorable tissue compatibility, yttria-stabilized zirconia (YSZ) have been well-received in prosthodontics in form of dental implants, abutments, crowns and bridges [1,2]. Notably, aesthetic values of YSZ, including peri-implant mucosal aesthetic effects and mimics natural tooth-like color, make YSZ the preferred substitute for implants and crowns where esthetics are required [3]. Nevertheless, early bone-implant integration is hampered by bio-inert interface of YSZ [4], while the same dilemma also accounts for the inadequate bond between YSZ and porcelain veneer or resin cement as well as fails to provide an ideal retention of dental restorations, which typically causes the failure of the clinical prothesis [5]. Hence, there is a growing interest in surface modification techniques aimed at extending the working life of YSZ implants and prostheses.

To further enhance micromechanical retention and osseointegration,

---

Peer review under the responsibility of editorial board of Bioactive Materials.

* Corresponding author. Shangcai Village, Nanbaixiang Street, Ouhai District, Wenzhou City, Zhejiang Province, China.
** Corresponding author. 51# Xuefu Road, Yinzhou District, Ningbo City, Zhejiang Province, China.
*** Corresponding author. 268# Xueyuan West Road, Lucheng District, Wenzhou City, Zhejiang Province, China.
E-mail addresses: lihuaxu@wmu.edu.cn (L. Xu), shenxinkun123@wmu.edu.cn (X. Shen), jinsong0719@wmu.edu.cn (J. Liu).

[1] Co-authors: These authors contributed equally to this work.

https://doi.org/10.1016/j.bioactmat.2025.03.028
Received 25 December 2024; Received in revised form 26 March 2025; Accepted 27 March 2025

past studies have capitalized on air-abrasion, etching and ultraviolet irradiation to improve the available surface area, roughness, and interface energy of YSZ [6–8]. However, these methods have limitations. Although they have achieved some progress in surface modification, they may not provide a strong enough bond to effectively prevent interface cracking between YSZ and porcelain veneer or between YSZ and resin cement [9]. Notably, sandblasting treatment has been found to introduce defects, particularly those that involve plastic deformation [10]. On the other hand, the construction of nanostructure and insertion of functional groups on YSZ surface can not only strengthen the interfacial interlocking between YSZ and regenerated new bone, but also provide a suitable microenvironment for regulating cell behavior and bone remodeling [11,12]. And meanwhile, these structures also contribute to micromechanical retention as well as hydrogen bonding at the interface of YSZ and porcelain veneer or resin cement [13,14]. It is commonly recognized that the technologies of laser texturing, plasma spray and peptide grafting are generally used for preparation of micro-pattern and bioactive coatings on YSZ [15–17]. Unfortunately, during the modification process, potential problems may arise, such as over-sandblasting leading to ceramic chipping, hydrofluoric acid causing damage to soft tissues and teeth, and the high cost and complex operation of using laser instruments [18,19]. As such, there is an urgent demand for an approach that is practical, cost-effective, and non-irritating to achieve an ideal YSZ surface.

As one of nature's masterpieces, the forewings of the *Allomyrina dichotoma* beetle are both lightweight and stiff, serving functions of self-protection and flight support [20]. The core structure of the elytra is firm and highly intensive which were given large surface area, resistance to mechanical deformation, high fracture toughness, impact protection as well as energy dissipation, utilizing various energy-dissipating mechanisms across multiple length scales [21,22]. Inspired by the unique composite structure found in the elytra, Du et al. developed biomimetic alloy tubes demonstrating superior energy absorption, dissipation, and impact resistance [23]. A similar damping behavior exists in the periodontal ligaments (PDL) surrounding natural teeth for dispersing and transferring occlusal forces [24]. Unfortunately, the current implant system, lacking in a natural "damping layer" like PDL, is more susceptible to the progressive peri-implant bone loss [25]. Therefore, it is necessary to construct an energy-dissipation interfacial layer acting as an artificial PDL between implants and surrounding bone to weaken the impact load. On the other hand, the design of a damping layer in ceramic prostheses also enhanced energy dispersion and increased the bonding strength at the adhesive interface, further improving the long-term performance of implant-supported prostheses [26,27]. However, there is no report on the systematic application research of this biomimetic damped structure in ceramic-prosthesis repair.

Inspired by the microstructure of the elytra core, an innovative design concept for fabricating integrated biomimetic trabecular-honeycomb nanonetwork on YSZ surface is herein demonstrated. By facile hydrothermal reaction, we successfully obtained YSZ with a surface biomimetic nanonetwork of self-assembled zirconium phosphate (ZrP) which not only mimicked critical features of the elytra core but also exhibited superior energy-dissipation capability, great hardness and high strength. Furthermore, ZrP nanonetwork endows YSZ surface with abundant phosphate groups, which act synergistically with the nanotopographical features for not only reinforcing the bonding strength at the interface of YSZ and porcelain veneer/resin cement, but for promoting the osteogenic differentiation *in vitro* and the bone regeneration *in vivo*. Additionally, the ZrP nanonetwork modulates the immune microenvironment, activating macrophage polarization towards the pro-healing M2 phenotype, thus synergistically stimulating bone regeneration *in vivo*. This study demonstrates that YSZ with the self-assembled zirconium phosphate (ZrP) biomimetic nanonetwork on the surface overcomes the current challenges in physicochemical modification of zirconia surfaces, making a valuable contribution to the expanded application of zirconia in dental implants and dental defect restoration (Scheme 1).

2. Experimental section

2.1. *Preparation of trabecular-honeycomb ZrP nanonetwork on yttria-stabilized zirconia ceramic*

Commercially available 3 % yttria-stabilized zirconia (YSZ) ceramics (Shenzhen Upcera Dental Technology Co., LTD.) were divided and sintered into 10 × 10 × 1.5 mm. The sintering protocol comprised two stages: heating the specimens to 900 °C at 5 °C/min (with a 30-min dwell time), followed by a second heating phase to 1530 °C at 3 °C/min with a 4-h hold. After sintering, specimens were sequentially polished to mirror-like finish using 400, 600, 800, and 1000 grit waterproof abrasive papers and ultrasonically cleaned with acetone, ethanol, and ultrapure water.

The trabecular-honeycomb nanonetworks (designated as ZrP-YSZ) were fabricated on the polished YSZ surfaces via hydrothermal treatment. In short, polished YSZ specimens were respectively immersed in H_3PO_4 solutions (0.5, 1.0, 2.5, and 5.0 wt%) and heated at 80, 120, and 160 °C for 24 h. After hydrothermal processing, these nanonetworks modified YSZ specimens underwent a second sintering treatment at 950 °C for 15 min, assigned to SS-ZrP-YSZ group. The sandblasting group (SL-YSZ) served as the clinical control, which was obtained by polishing YSZ and subsequently treating with 110 μm alumina particles at 0.3 MPa pressure through sandblasting, without hydrothermal treatment.

2.2. *Characterization of surface physicochemical properties*

The surface color of each sample was photographed using a digital camera (Canon EOS 800D, Japan). The surface and cross-sectional morphologies, as well as the roughness of different groups, were analyzed using a field-emission scanning electron microscope (FE-SEM, Hitachi SU8010) and an atomic force microscope (AFM, Bruker Dimension ICON), respectively. Additionally, the pore size and thickness of the ZrP nanonetwork were measured and quantified using Image Pro software. X-ray photoelectron spectroscopy (XPS, Thermo ESCALAB 250XI) and X-ray energy dispersive spectrometer (EDS, Hitachi S4800) were employed to survey the chemical composition of the ZrP nanonetworks. Zr 3d, O 1s, P 2p, and Y 3d were further scanned and surveyed by high-resolution XPS. The crystallization phases of modified YSZ were viewed by UV Raman spectroscopy (Renishaw inVia) at an excitation wavelength of 480 nm and X-ray diffractometer (BrukerD-8) using with Cu Kα radiation source ($\lambda = 1.5406$ Å). The wettability of modified YSZ was measured by using a contact angle meter (SDC-200S) for collecting water contact angle images.

2.3. *Mechanical properties*

According to ISO 6872:2015, a three-point flexural test was taken to assess flexural strength utilizing the electronic universal testing machine (Instron 2716–020). In general, test specimens were put in clamps with a span of 20 mm and loaded at a crosshead speed of 0.5 mm/min until the specimens failed. A rockwell superficial hardness tester (Time TH320) was conducted to measure the hardness of materials. A load force of 60 kg was applied on the specimens' surface and maintained for 10 s by using a 120° diamond conical indenter.

2.4. *Nano-dynamic mechanical analysis (Nano-DMA)*

The dynamic energy dissipation, Young's modulus and nanohardness of the ZrP nanonetwork were assessed by the Nano-dynamic mechanical analyzer (Hysitron TI980) within a frequency range of 10 Hz–110 Hz. A maximum loading of 10 mN was applied to specimens for 10 s and tan δ values were recorded to evaluate the energy-dissipation

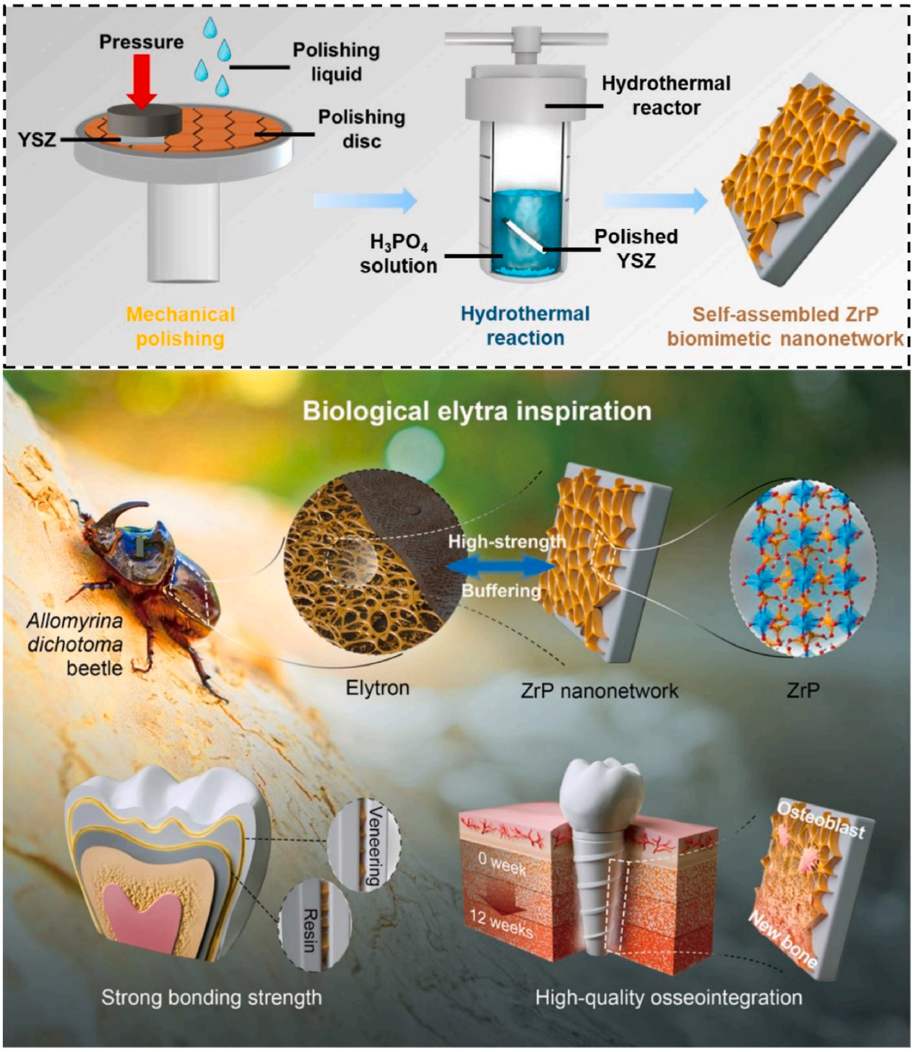

Scheme 1. Schematic diagram of the fabrication process of bioinspired beetle elytra ZrP nanonetwork modified YSZ which offers high-quality interface bonding strength and superior osteogenesis *in vivo* for zirconia restorations and implants respectively.

capacity of the ZrP nanonetwork.

2.5. Nanoscratch test

Nanoscratch test was applied to quantitatively assess the coating-substrate adhesion under progressive loading (0–200 mN) by a nanoscratch tester (Bruker Hysitron TI980), with the critical load (Lc) defined as the minimum force required to initiate coating delamination.

2.6. Veneering procedures

Firstly, powder and liquid were mixed in proportion as indicated. Subsequently, the cylindrical porcelain veneer (Vita, VM®9 5M3) of 4 mm in diameter as well as 5 mm in height was shaped on the surface of YSZ through a silicon rubber mold. After removing the mold, the porcelain veneer was programmatically sintered according to the manufacturer's instructions.

2.7. Cementation protocols

To evaluate the bonding strength between resin cement and zirconia, a standard mold with 4 mm in bottom diameter and 5 mm in height was laced on the specimens to equalize the bonding area. Resin cement (3M ESPE, RelyX™ Unicem Aplicap™) was mixed strictly to the instructions, and then evenly filled into the mold. After curing for short exposure, the spilled cement was removed, followed by curing the adhesive edge for 20 s.

2.8. Shear bonding strength (SBS) test

The assembled specimens were fixed on the jig and fixture, and then subjected to the electronic universal testing machine. A load of blade like tips was applied at a uniform speed of 0.5 mm/min parallel to the bonding interface until the porcelain or resin cement was stripped from the YSZ. The shear stress-displacement curves were plotted by the computer in the course. Simultaneously, the peak shear stress when the fracture occurred was recorded in Newton. And shear stresses were calculated by the Formula I:

$$\text{Shear stress (MPa)} = \text{Shear force (N)} \Big/ \text{bonding area} \left(\text{mm}^2\right) \qquad \text{(Formula I)}$$

2.9. Fracture mode ratio analysis

We analyzed fracture modes using an optical stereomicroscope (40 × magnification) and classified them based on the interfacial fracture area ratio (FAR), which was calculated by the Formula II:

$$\mathrm{FAR}\ (\%) = (\text{Delaminated area} / \ \text{Total bonded area}) \times 100\% \qquad \text{(Formula II)}$$

2.10. *Assessment of the osteogenic potential in vitro*

MC3T3-E1 cell line (ATCC CRL-2594) was cultured in α-minimum essential medium (α-MEM, HyClone, China) complemented with 10 % fetal bovine serum (FBS, BioInd, Israel) and 1 % penicillin-streptomycin mixture (Gibco, America) until the cell density reached 80 %–90 %.

About the cell morphology research, MC3T3-E1 cells were seeded on specimens at the density of 5×10^3 cells per well in 24-well plates. After 2 d of incubation, the adherent cells were fixed by 4 wt% paraformaldehyde solution, and subsequently, the actin cytoskeleton and nucleus were stained with FITC-phalloidin (Solarbio, China) and DAPI (Yeasen, China), respectively. The fluorescence microscope (Nikon, Japan) was subjected to photograph cell morphology. At least 4 samples were collected from each group and the cell aspect ratio/area were calculated by Image J software.

MC3T3-E1 cells were incubated on materials with an initial cell density of 2×10^4 per well in 24-well plates. Cell Counting Kit-8 (CCK-8, Dojindo, Japan) was used to test the cell viability after 1 d, 4 d, and 7 d of culture. The osteogenic medium (supplement with 10 mM β-glycerophosphate, 0.1 mM dexamethasone, and 0.05 mM ascorbic acid) was replaced every other day, and the assays of alkaline phosphatase (ALP) activity and the mineralization level were separately at 4 d and 14 d. Furthermore, alkaline phosphatase assay kit (Beyotime, China) and alizarin red S dye (ARS, Solarbio, China) along with 1 wt% cetyl pyridinium chloride (Sigma, America) were used for the quantitative assay of osteogenic abilities, before which ARS dyeing mineralization nodules were photographed by the optical stereomicroscope.

The relative gene expression levels of osteogenesis including *runt-related transcription factor 2* (*Runx2*), *alkaline phosphatase* (*ALP*), and *osteocalcin* (*OCN*) were detected by quantitative reverse transcription-polymerase chain reaction (qRT-PCR). After incubation for 7 d at a preliminary density of 2×10^4 cells per well, MC3T3-E1 cells were gathered to extract total RNA by using of an RNA extraction kit (Takara RNAiso Plus, Japan). The RNA concentration of each group was further measured by the NanoDrop 2000 micro-spectrophotometer (Thermo Scientific, America). If the A260/A280 ratio of extracted RNA was laid with 1.8–2.0, a reverse transcription process would be performed to synthesize cDNA using a PrimeScript RT Reagent Kit (Takara, Perfect Real Time, Japan). Finally, the expression level of osteogenic-related genes was measured on the StepOnePlus Real-Time PCR System (Thermo Scientific, America) by applying a TB Green Premix Ex Taq II kit (Takara Tli RNaseH Plus, America). The primer sequences of *Runx2*, *ALP*, *OCN*, and *glyceraldehyde phosphate dehydrogenase* (*GAPDH*) genes were listed in Table S4, Supporting Information, in which *GAPDH* was designated as the housekeeping gene. In addition, the protein expression levels of Runx2 and OCN in MC3T3-E1 cells were further determined by Western blotting (WB) test.

2.11. *Assessment of the immune regulation in vitro*

RAW 264.7 macrophages (ATCC TIB-71) were cultured in the high-glucose Dulbecco's Modified Eagle's Medium (DMEM) supplemented with 10 % FBS to assess the osteoimmune regulatory capabilities of ZrP nanonetworks with varying pore sizes *in vitro*. RAW 264.7 cells were seeded at a density of 1 × 10^4 cells per well in a 24-well plate and, after 24 h of incubation, were subjected to fluorescence staining and cell morphology observation following previously outlined methods.

Flow cytometry was adopted to assess the proportions of M1 and M2 phenotype macrophages on the sample surfaces. After co-culturing RAW 264.7 macrophages with different samples for 3 d, the collected macrophages were then incubated with APC-conjugated CD86 antibodies (Biolegend, 105012, 1:100) and FITC-conjugated CD206 antibodies (Biolegend, 141703, 1:100) to specifically label M1 and M2 macrophages, respectively. Subsequently, the expression levels of M1 and M2 markers were detected using a flow cytometer (Agilent, NovoCyte, USA) and the data were analyzed with the NovoExpress software (Version 1.4.1, USA).

To further investigate the effects of ZrP nanonetworks with varying pore sizes on the expression of immune-related genes in macrophages, RT-qPCR analysis was performed. Following a five-day co-culture of macrophages with ZrP nanonetworks, total RNA was extracted and reverse transcribed into cDNA. Subsequently, qRT-PCR was conducted using specific primers to assess the relative gene expression levels of osteogenic markers (*Runx2* and *BMP-2*), pro-inflammatory cytokines (*IL-6* and *iNOS*), and anti-inflammatory cytokines (*IL-10* and *CD163*). The sequences of the relevant primers are detailed in Table S4 of the Supporting Information. Moreover, the protein expression level of CD206 (M2 marker) were further determined by WB test.

2.12. *Evaluation of the osteogenesis in vivo*

All animal experiments carried out in the Animal Experiment Center of Wenzhou Institute of Biomaterials and Engineering were approved by the Animal Ethics Committee of Wenzhou Institute University of Chinese Academy of Sciences (Approval number: WIUCAS22111001), which were strictly following the ethical and welfare requirements of the center during experiments. In considering the above results of physicochemical properties and osteogenic potential *in vitro*, YSZ, SL-YSZ, SS-160°C(1.0%), and SS-160°C(2.5%) were chosen for the animal experiments. Twenty male Japanese white rabbits (22–24 weeks, 2.5–3.5 kg) were randomly divided into four groups. First, the rabbits were administered 30 mg/mL of pentobarbital sodium through ear veins for general anesthesia. Then, a longitudinal incision (2 cm) was made centered on the medial epicondyle of the femur and subsequently, the cylindrical bone defect was prepared by surgical drills with different diameters in the step-by-step routine. Finally, the specimens with a cross-sectional diameter of 4 mm and a length of 10 mm were implanted into the socket, moreover, the tissue was sutured layer by layer.

Four weeks after the operation, the rabbits were executed with an overdose of anesthetic and femoral condyles were collected as well as fixed. After dehydrating by graded ethanol, undecalcified samples were embedded with photopolymer resin (EXAKT, TL7200 VLC, Germany). Then, a hard tissue slicer (EXAKT 300CP, Germany) was applied to slice along the axis of the implants. Hard tissue slices were ground to the final thickness of 20 μm and these histological images stained by Masson's trichrome staining were gathered through the optical stereomicroscope and upright microscope. Quantitative histomorphological analyses were performed by Image Pro Plus to assess the proportion of mature bone (mature bone/the area of ROI) and the percentage of bone-implant contact (BIC %) in a selecting 4 mm × 0.5 mm region of interest around implants (ROI).

To assess the bonding strength between the implants and bone tissue across different groups, pullout tests were conducted. All samples were tested with an electronic universal testing machine (MTS EXCEED MODEL E43, China). During testing, a constant tensile rate of 10 mm/min was applied to the implants until failure and detachment from the bone tissue. The maximum load at failure was recorded as the maximum pullout force, serving to quantify the differences in bonding strength among the groups. And the extracted implants were undergoing CO_2 supercritical freeze-drying and gold coating. The micro-morphology and elemental composition of the implant-femur failure interface were then assessed using the SEM coupled with EDS.

2.13. *Statistical analysis*

All data were graphed by Origin 2018 and analyzed by IBM SPSS Statistics 22.0. The normality assessment of the data was tested using the Shapiro-Wilk normality test. If the data didn't meet the normal distribution, it was then transformed to be normally distributed. Quantitative data were expressed as a form of Mean ± standard deviation (Mean ± SD), and one-way ANOVA was employed for difference comparison among groups. The *p*-value less than 0.05 ($*p < 0.05$) was considered that there was a significant difference.

3. Results and discussion

3.1. Self-assembly of integrated biomimetic trabecular-honeycomb nanonetwork

We have achieved a significant breakthrough in the self-assembly of nanostructures on polycrystalline tetragonal YSZ, as previously only self-assembled nanostructures on single crystal YSZ surfaces had been reported. The widespread application of single crystal YSZ is generally constrained by its high cost and complex operational procedures [28]. In this work, we proposed a novel approach in which the ZrP nanonetwork self-assembled on the YSZ block surface using the H_3PO_4 aqueous solution. Crucially, we found that the pore size of the self-assembled structure could be tailored by varying the reaction temperatures and phosphoric acid (H_3PO_4) concentrations (Fig. 1a). The microstructure of the ZrP nanonetwork closely resembled the core structure of beetle's elytra, presenting a trabecular-honeycomb composite structure (Fig. 1b). The self-assembly process and subsequent nanonetwork formation were influenced by pH, which was predominantly controlled through H_3PO_4 concentration gradients. Our experiments indicated that when the final mixed reaction solution kept a pH below 1.25, complete suppression of nanonetwork assembly was observed in the 80°C(5.0%) and 120°C(5.0%) groups. Within the final pH range of 1.25–1.40, sporadic nanosheet nucleation occurred, which correlated with defective nanonetwork in the 80°C(2.5%) and 160°C(5.0%) groups. When the pH exceeded 1.66, discontinuous nanonetwork formation and structural

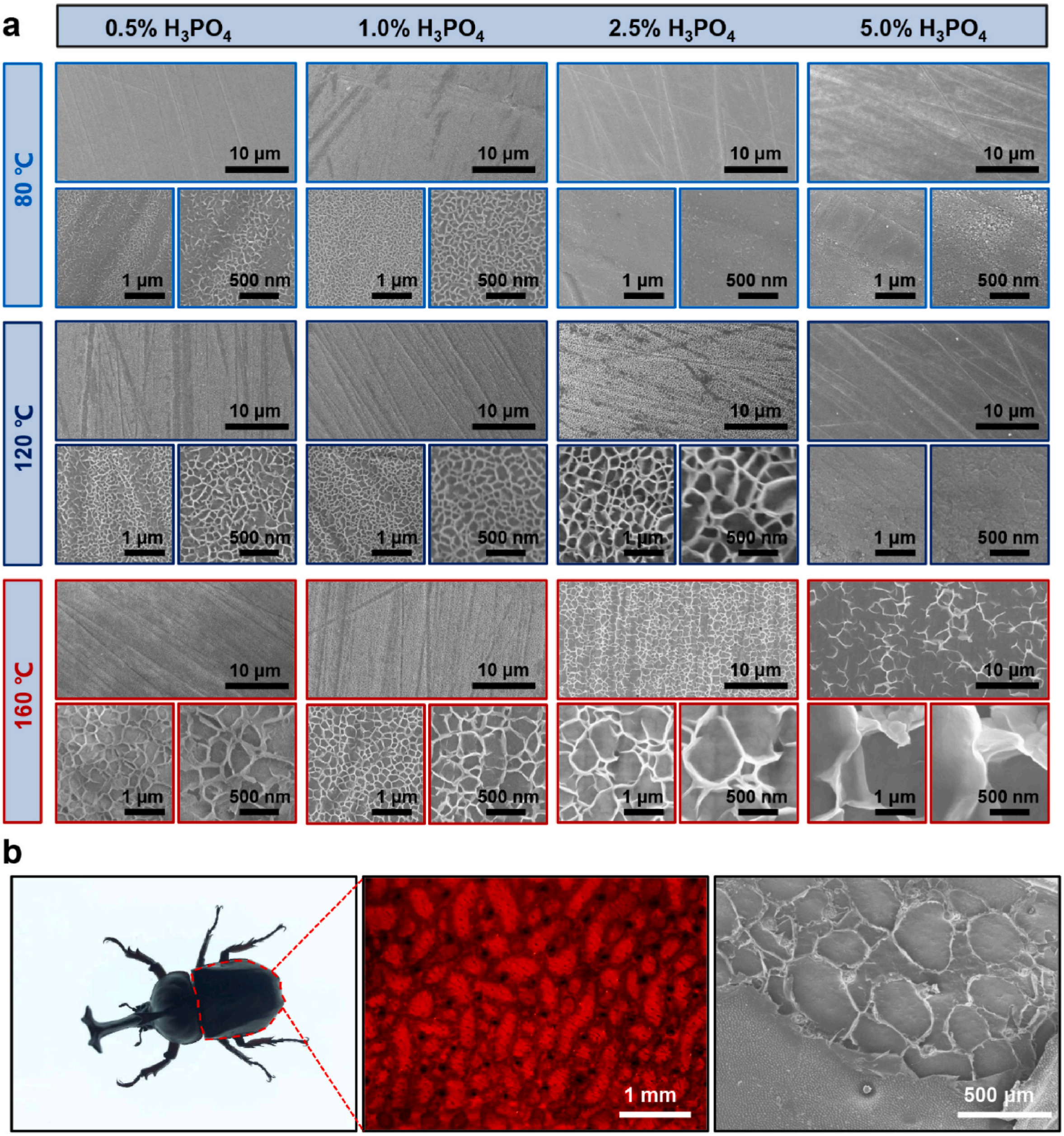

Fig. 1. The microstructure of elytra-bioinspired self-assembly ZrP nanonetwork by adjusting the reaction temperature and the concentration of H_3PO_4. a) Scanning electron microscope (SEM) images of the ZrP-YSZ at varying H_3PO_4 concentrations (0.5, 1.0, 2.5, and 5.0 wt%) and different reaction temperatures (80, 120, and 160 °C). b) Details of the beetle elytron photographed by a digital camera (left), stereomicroscope (middle), and SEM (right).

collapse appeared in the 120°C(0.5%) and 160°C(0.5%) groups (Table S1, Supporting Information). Trabecular-honeycomb networks were obtained in 80°C(0.5%), 80°C(1.0%), 120°C(0.5%), 120°C(1.0%), 120°C(2.5%), 160°C(0.5%), 160°C(1.0%) and 160°C(2.5%) groups with an average pore size of 16.4, 24.5, 38.0, 52.0, 111.8, 78.1, 203.6 and 600.8 nm, respectively (Fig. 1a and S1, Supporting Information). We observed that the final pore size was positively related to reaction temperatures and showed a trend of enlarging with an increase of H_3PO_4 in limited concentration.

Overall, the self-assembly of ZrP nanonetworks is governed by synergistic interactions between reaction thermodynamics and pH equilibrium. I) Elevated temperatures (120 °C–160 °C) accompanied by the gradual rise in pressure within pressurized reactors (Table S2, Supporting Information) accelerate the ionization of H_3PO_4, rapidly dissolving Y^{3+} ions and zirconium (Zr^{4+}) ions from YSZ to initiate ZrP nucleation [29]. II) While temperatures below 80 °C impede Zr^{4+} dissociation, excessive temperatures induce irregular ZrP structure [30]. III) Optimal concentrations of H_3PO_4 (1.0 wt% - 2.5 wt%) induces the generation of abundant ZrP nuclei, providing templates for ordered self-assembled nanonetwork. IV) High concentrations of H_3PO_4 (exceeding 5.0 wt%) causes low degree of ionization, significantly inhibiting the production of uncondensed Zr-OH groups while inducing nuclei dissolution, thus limiting ZrP growth and maturation [31]. The self-assembly process of ZrP follows the dissolution–precipitation dynamics and Ostwald ripening mechanism [32], where larger ZrP grains grow quickly at the expense of smaller ones. At 160 °C with 2.5 wt% H_3PO_4, accelerated ripening generates a nanonetwork with the largest pore size (600.8 ± 186.4 nm), mimicking the trabecular-honeycomb structure of load-bearing elytra. By strategically balancing temperature and H_3PO_4 concentration, we achieved precise pore size modulation, demonstrating tunable structural control. Based on the screening of experimental results, 120°C(1.0%), 120°C(2.5%), 160°C(1.0%) and 160°C(2.5%) groups were identified as the optimal preparation parameters for the ZrP nanonetwork, collectively referred as ZrP-YSZ. Moreover, according to pore size, they were divided into the small-pore-size [120°C(1.0%)], medium-pore-size [120°C(2.5%) and 160°C(1.0%)], and large-pore-size [160°C(2.5%)] groups.

EDS spectroscopy confirmed the uniform distribution of Zr, P, and O elements on the ZrP-YSZ specimens, with complete absence of P signals in both YSZ and SL-YSZ controls (Fig. S2, Supporting Information). The SL-YSZ sample displayed Al signals due to residual alumina particles. To further identify the element compositions and their oxidation state of the ZrP nanonetwork arose from the hydrothermal process of H_3PO_4 and YSZ, high resolution XPS was carried out to characterize ZrP-YSZ (Fig. 2a and S3, Supporting Information). The major presence of 182.1 and 184.4 eV peaks in the Zr 3d spectra could be allocated to Zr $3d_{5/2}$ and Zr $3d_{3/2}$ of Zr^{4+} respectively. After H_3PO_4 hydrothermal treatment of ZrP-YSZ groups, the resulting shift to higher Zr 3d binding energy was attributed to the appearance of P-O-Zr bonding, while the signal of P 2p at 133.8 eV derived from the P-OH linkage and its intensity increased with elevated concentration of H_3PO_4. Moreover, the O 1s spectra figured out that O 1s shifted to higher binding energies ZrP-YSZ groups, following the variable co-ordination mode that Zr-O-Zr and Y-O-Y linkage at 529.7 eV increasingly changed to Zr-O-P linkage at 531.2 eV. But meanwhile, the areas of Y 3d signal at 157.4 and 159.4 eV were significantly reduced suggesting that yttria dissolved in the H_3PO_4 hydrothermal process. Higher temperatures and H_3PO_4 concentrations made positive contribution to the atomic ratio of P/Zr (Table S3, Supporting Information), and the ascending atomic ratio of P/Zr exhibited more phosphate groups incorporated into the nanonetwork. Fig. 2b displayed the Raman spectrum of YSZ and ZrP-YSZ groups. The characteristic bands at 146, 260, 323, 464, and 642 cm^{-1} proved the presence of the tetragonal phases (ZrO_2-t) of YSZ [33], denoted by triangle symbols. The formation of surface ZrP nanonetworks was at the expense of tetragonal zirconia, resulting in the formation of a large number of monoclinic phase zirconia (ZrO_2-m) which were labeled as by circle symbols. Based on the XPS and Raman spectra, we preferred the surface ZrP nanonetwork is likely amorphous ZrP. Then, the changes in surface roughness and vertical height across different groups were examined by AFM (Fig. 2c and S4a, Supporting Information), revealing the significant influence of the nanonetwork structure on surface morphology. Compared to the smoother YSZ and the relatively rough SL-YSZ group, the ZrP-YSZ groups displayed distinct surface roughness characteristics correlated with pore size. Specifically, as the nanonetwork pore size increased, both surface roughness and vertical height showed significant enhancement, with the large-pore-size group achieving the maximum roughness (Ra = 65.1 ± 18.2 nm) and peak vertical height (184.9 ± 31.1 nm). Further statistical analysis of SEM images revealed that the wall thickness of ZrP-YSZ nanonetworks significantly increased with pore size enlargement, showing the same trend to AFM vertical height measurements, where the large-pore group exhibited a maximum wall thickness of 14.6 ± 5.1 nm (Fig. S4b, Supporting Information). The observed trend could result from the elevated reaction temperatures and H_3PO_4 concentrations, which facilitated pore larger pore sizes and the self-assembly of more phosphate groups into ZrP structures, thereby increasing surface complexity. Increased surface roughness offers additional binding sites for protein adsorption and establishes favorable conditions for subsequent cell adhesion onto the nanonetwork surface [34].

The time-dependent self-assembly development of ZrP nanonetwork in 2.5 wt% H_3PO_4 at 160 °C was investigated by SEM characterization (Fig. 2e). During the initial phase (3 h), heterogeneous nucleation predominantly generated amorphous ZrP nuclei on YSZ surface, while monoclinic laths served as preferential secondary nucleation sites, driving the self-assembly of ZrP nanorods and enabling their oriented growth on the YSZ substrate. As hydrothermal treatment progressed to 6 h, these nanorods exhibited anisotropic growth along the crystallographic planes of the monoclinic phase, coalescing into nano-laminar structures through edge-to-face crosslinking. By 12 h, a partially crosslinked ZrP nanonetwork with smaller pore sizes had formed. Upon extending the reaction to 24 h, the Ostwald ripening process drove the nanonetwork toward enhanced structural integrity, where smaller curvature radius of ZrP grains dissolved and recrystallized into larger grains, resulting in larger pore sizes. This morphological evolution from amorphous precursors to ordered trabecular-honeycomb nanonetworks conclusively demonstrates Ostwald ripening as the governing mechanism directing the self-assembly of ZrP nanonetwork [35].

A template-free self-assembly mechanism for ZrP nanonetwork, giving the example of 160°C(2.5%) group, is proposed (Fig. 2d). The progression involves complex physicochemical transformations, including ions release, nucleation, martensitic phase transformation, oriented attachment growth of nano-laminar ZrP induced via Ostwald ripening, and the self-assembly of nanonetwork. Initially, hydrothermal treatment triggers rapid hydrolysis of YSZ surface to release Zr^{4+}, which undergo rapid complexation with hydrogen phosphate ions (HPO_4^{2-}) to drive the self-assembly of ZrP nuclei at the liquid-gas interface. Concurrently, hydrothermal conditions facilitate the tetragonal to monoclinic (t→m) phase transformation in YSZ, generating monoclinic zirconia (ZrO_2-m) domains [36]. These transgranular ZrO_2-m domains serve as templates of secondary nucleation [37], mediating intercalation-type interactions between $Zr(OH)_2^{2+}$ and HPO_4^{2-}, thereby driving the oriented attachment growth of ZrP nuclei along monoclinic crystallographic planes into nanorods [38]. Subsequently, ZrP nanorods rapidly undergo anisotropic growth into larger nano lamellas via Ostwald ripening dynamics, where smaller particles dissolve to recrystallize into larger crystals [35]. Meanwhile, acid-mediated edge protonation triggers edge-to-edge and face-to-edge stacking between adjacent ZrP nano lamellas through hydrogen bonding and van der Waals forces, while microphase-separated domains at the liquid-gas interface guide the spontaneous formation of trabecular-honeycomb nanonetworks [39, 40].

To ensure strong bonding of the ZrP nanonetwork to the YSZ

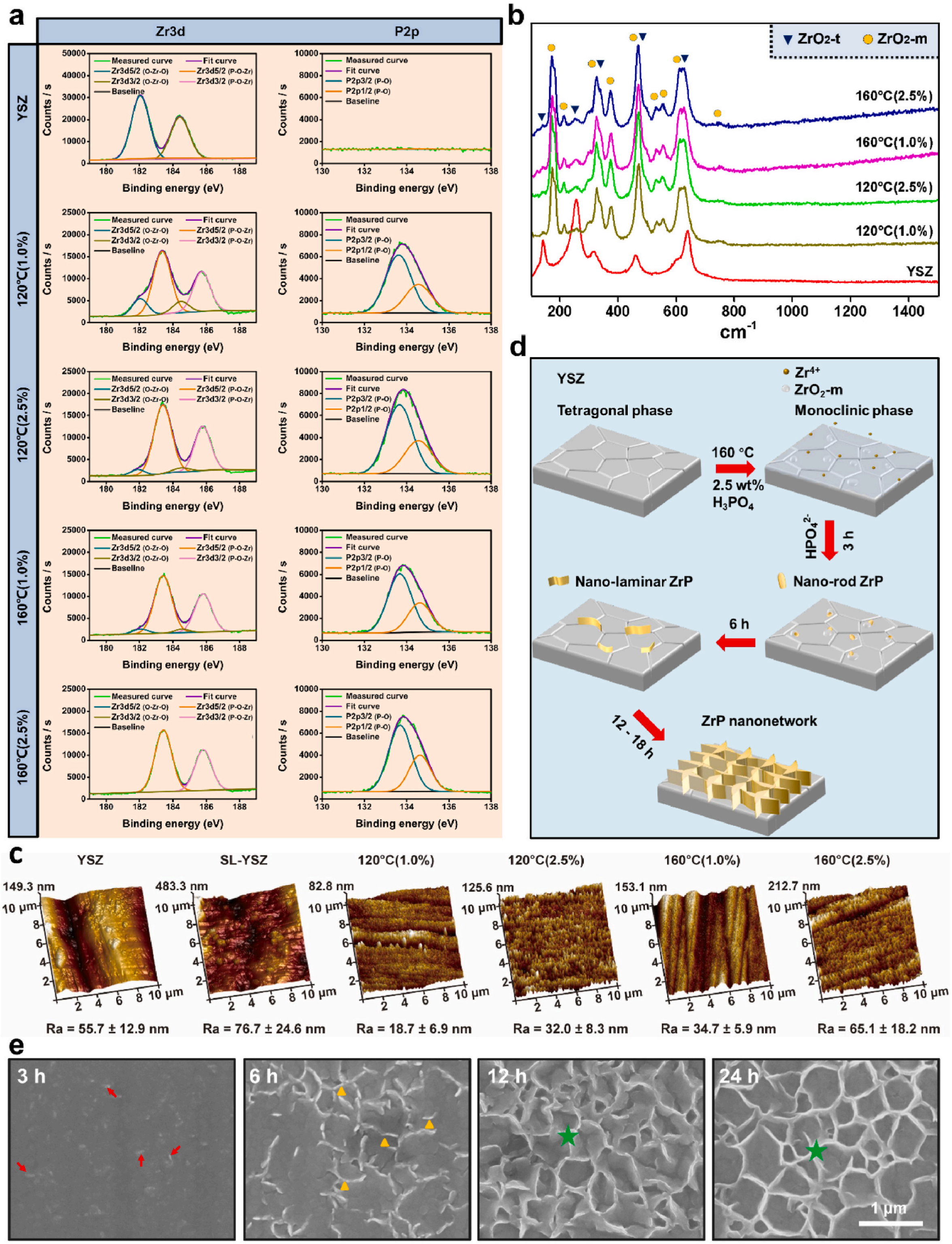

Fig. 2. The formation mechanism of elytra-inspired trabecular-honeycomb zirconium phosphate (ZrP) nanonetwork as inferred from the chemical composition and phase transformations. a) Fitted XPS spectra of Zr 3d and P 2p of YSZ and ZrP-YSZ. b) Raman spectrum of YSZ and ZrP-YSZ. The triangles and circles separately indicate the Raman bands of the tetragonal zirconia (ZrO_2-t) and monoclinic zirconia (ZrO_2-m). c) Representative AFM images of each group and surface roughness obtained from AFM analysis (n = 3 samples per group). d) The scheme of ZrP self-assemble into trabecular-honeycomb nanonetwork on YSZ surface, of which the process mainly includes Zr^{4+} releasing, the formation of monoclinic zirconia (ZrO_2-m), ZrP intercalative binding and lamellar growth via Ostwald ripening mechanism as well as trabecular-honeycomb nanonetwork formation. e) The surface morphology transition of 160°C(2.5%) specimens after H_3PO_4 hydrothermal treatment for 3, 6, 12, and 24 h. The red arrow represents nano-rod ZrP, the yellow triangle represents nano-lamellar ZrP, and the green pentagram represents ZrP nanonetwork. [Abbreviations: YSZ, yttria stabilized zirconia; SL-YSZ, sandblast the surface of YSZ; ZrP-YSZ, ZrP nanonetwork modified YSZ including 120°C(1.0%), 120°C(2.5%), 160°C(1.0%) and 160°C(2.5%) groups.].

substrate, a second sintering treatment was performed on hydrothermal-treated ZrP-YSZ samples. These second-sintered samples were designated as SS-ZrP-YSZ and categorized into SS-120°C(1.0%), SS-120°C (2.5%), SS-160°C(1.0%) and SS-160°C(2.5%) groups. SEM images revealed that both ZrP-YSZ and SS-ZrP-YSZ groups featured surfaces characterized by the ZrP nanonetwork of gradient pore sizes, and the second sintering process had minimal effect on the pore size and surface topography for ZrP nanonetwork (Fig. 3a). Consequently, the SS-ZrP-YSZ samples were similarly classified into small-pore-size [SS-120°C (1.0%)], medium-pore-size [SS-120°C(2.5%) and SS-160°C(1.0%)], and large-pore-size [SS-160°C(2.5%)] groups. Optical images demonstrated the retention of aesthetic properties in SS-ZrP-YSZ groups following hydrothermal treatment and the second sintering treatment, with all experimental groups maintaining clinically acceptable coloration comparable to conventional dental-grade zirconia (Fig. S5, Supporting Information). Moreover, the average thickness of the nanonetwork was estimated to be approximately 0.2 μm from the cross-sectional scanning electron microscope images (Fig. S6, Supporting Information). When

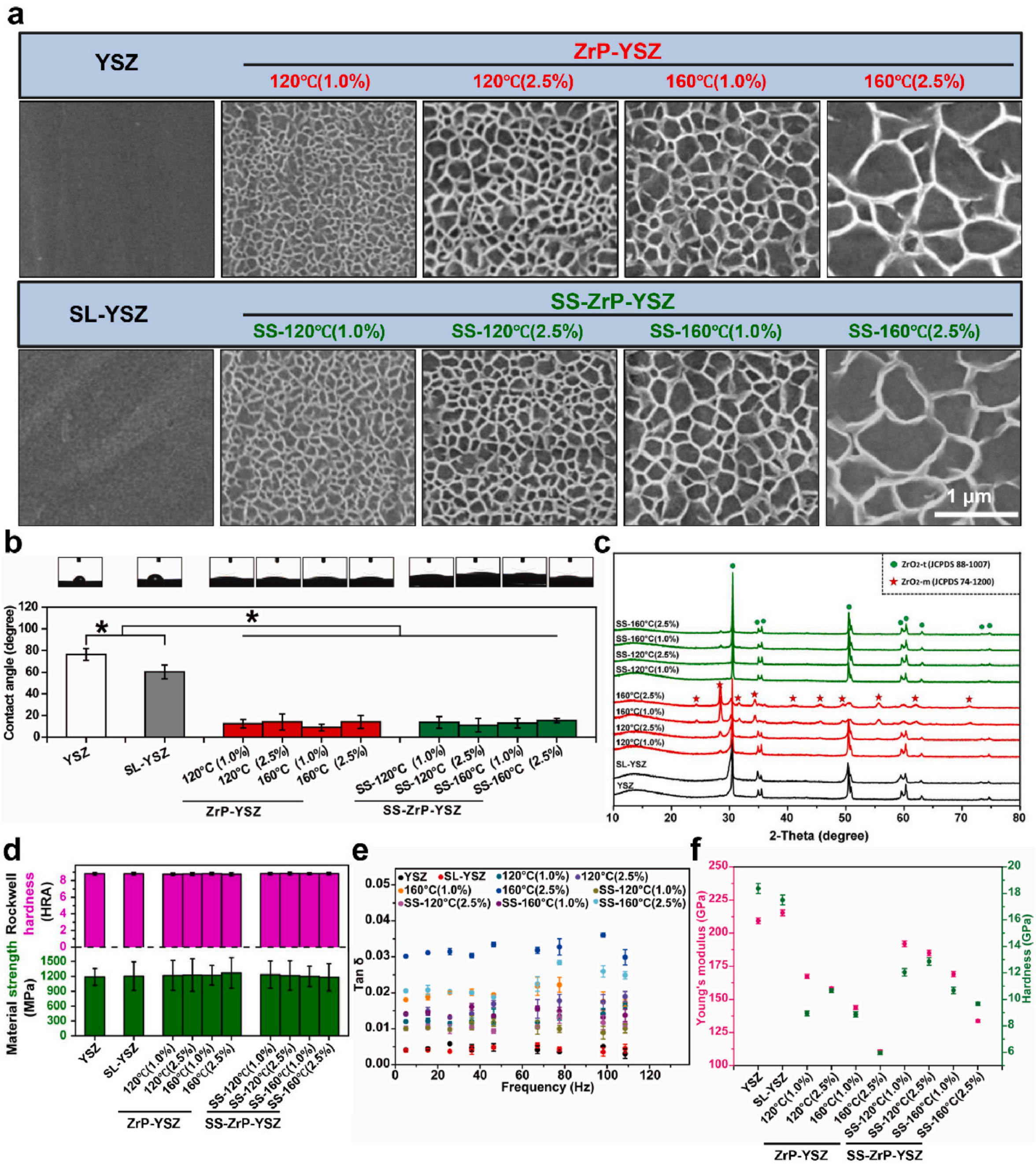

Fig. 3. The surface characterization, mechanical properties, dynamic energy dissipation and micro-mechanical properties of ZrP-YSZ and SS-ZrP-YSZ. a) Scanning electron microscope (SEM) images of YSZ, SL-YSZ, ZrP-YSZ, and SS-ZrP-YSZ. b) The water contact angle statistics and representative graphs of different groups. c) X-ray diffraction (XRD) patterns of different groups. The circles and asterisks indicate the tetragonal zirconia (ZrO_2-t) and monoclinic zirconia (ZrO_2-m), respectively. d) The statistical graphic of Rockwell hardness (top) and flexural strength (bottom) of different groups. e) Nano-dynamic mechanical analysis measured the loss factor (tan δ) of different samples in the frequency range of 10 Hz–110 Hz. f) The statistical graph of surface Young's modulus and hardness of different samples. The error bars represent as mean ± SD (n = 3 samples per group). $^*p < 0.05$ represents a significant difference among groups. [Abbreviations: YSZ, yttria stabilized zirconia; SL-YSZ, sandblast the surface of YSZ; ZrP-YSZ, ZrP nanonetwork modified YSZ including 120°C(1.0%), 120°C(2.5%), 160°C(1.0%) and 160°C(2.5%) groups; SS-ZrP-YSZ, second-sintered ZrP nanonetwork modified YSZ including SS-120°C(1.0%), SS-120°C(2.5%), SS-160°C(1.0%) and SS-160°C(2.5%) groups.].

comparing the cross-sectional SEM images of the 160°C(2.5%) group to the YSZ group, it was confirmed that the trabecular-honeycomb nanonetwork did not alter the porosity of the YSZ matrix. In addition, the ZrP nanonetwork endowed YSZ with favorable hydrophilicity. Wettability experiments revealed that the water contact angle values of the ZrP-YSZ and SS-ZrP-YSZ groups were significantly lower compared to the YSZ and SL-YSZ groups (Fig. 3b). This improved hydrophilicity is primarily due to the abundant hydrophilic groups (e.g., hydroxyl) present on the ZrP nanonetwork, as well as its increased specific surface area and roughness. These combined factors reduce water contact angles, demonstrating that the ZrP nanonetwork substantially enhances the hydrophilicity of YSZ substrate. Improved surface hydrophilicity promotes early interaction between implant and blood, facilitating greater protein adsorption and improved cell adhesion. These effects synergistically support cell proliferation and osteogenic differentiation, ultimately leading to significantly improving implant osseointegration by establishing a biologically favorable environment [41].

X-ray diffraction (XRD) pattern (Fig. 3c) indicated that the crystallization peaks in YSZ and SL-YSZ groups dominated by tetragonal characteristic peaks of ZrO_2 (JCPDS 88–1007), while the monoclinic peaks (JCPDS 74–1200) appeared in ZrP-YSZ groups. The peak sites as well as intensities of monoclinic phase increased with the increasing hydrothermal temperature, especially in 160°C(1.0%) and 160°C(2.5%) groups by accelerating the reaction of H_3PO_4 and yttria and therefore promoting t→m transformation [42]. As for SS-ZrP-YSZ treated with second sintering, the second heat-treatment fully reversed the surface monoclinic phase to the tetragonal phase and helped stabilize the tetragonal phase ZrO_2. Such a transformation in crystalline phase could be ascribed to the migration of Y^{3+} to lower concentration areas on YSZ surface followed by thermally induced m→t phase transformation [43]. Furthermore, the mechanical properties of ZrP-YSZ and SS-ZrP-YSZ are hardly impacted by the short-term H_3PO_4 hydrothermal treatment and the subsequent second sintering. As shown in Fig. 3d, the Rockwell hardness (8.6–9.0 HRA) and flexural strength (900–1600 MPa) of ZrP-YSZ and SS-ZrP-YSZ groups were comparable to YSZ and SL-YSZ controls, confirming that bulk mechanical properties were preserved despite discrepancy in phase compositions. Cross-sectional SEM images revealed that the porous ZrP nanonetwork was constructed within a depth of ~0.2 μm in the surface layer, maintaining the compactness of the YSZ substrate. Hydrothermal treatment induced localized t→m phase transformation exclusively within this superficial zone, while preserving the tetragonal-phase-dominated YSZ bulk. Moreover, residual stress relief prevented subsurface defect propagation and maintained grain boundary cohesion [44]. This restricted phase transformation, combined with the compact YSZ substrate, ultimately preserved the flexural strength of the substrates.

As the load-bearing materials in oral, YSZ has long been subjected to dynamic loads. Here, the characteristics of dynamic energy dissipation of trabecular-honeycomb ZrP nanonetwork on YSZ were assessed by nano-dynamic mechanical analysis (Nano-DMA). Fig. 3e depicts the loss factor (tan δ)-frequency curves of various specimens in the frequency range 10 Hz–110 Hz, and all the loss factors of ZrP-YSZ and SS-ZrP-YSZ (0.010–0.032) are at least 2 times higher than those of YSZ (0.0044) and SL-YSZ (0.0041), among which 160°C(2.5%) shows the highest tan δ. As is expected, elytra-like ZrP nanonetwork could efficiently improve the energy-dissipation capacity owing to the impact resistant ability of trabecular-honeycomb structures. The other fascinating observation is that the loss factors of ZrP nanonetwork are lower with decreasing hydrothermal temperatures and H_3PO_4 concentrations as well as the resintering treatment, in accordance with the previous research that damping behavior could be induced by t→m martensitic phase transformation [45].

Subsequently, dynamic nano-indentation was employed to inspect the micro-mechanical properties of each group (Fig. 3f). Observations revealed that as the pore size increased, there was a decrease in the Young's modulus: for the ZrP-YSZ group, it declined from 170 GPa to 110 GPa. Similarly, for the SS-ZrP-YSZ group, it dropped from 190 GPa to 130 GPa. This is notably lower than the YSZ and SL-YSZ groups, which averaged around 210 GPa. The elastic modulus of the large-pore-size groups, especially the 160°C(2.5%) and SS-160°C(2.5%) groups, is approaching that of titanium [25]. Rockwell hardness measurements only reflect the macro-hardness of YSZ. Therefore, nanoindentation tests were conducted to characterize the nano-hardness of ZrP-YSZ and SS-ZrP-YSZ groups. The nano-hardness of both the ZrP-YSZ and SS-ZrP-YSZ groups was observed to be between 6 and 13 GPa, significantly less than that of the YSZ and SL-YSZ groups. The reduced nano-hardness and Young's modulus observed in the ZrP-YSZ groups, compared to the SS-ZrP-YSZ groups, were primarily attributed to their higher monoclinic phase content [46]. Elevated reaction temperatures and acid concentrations intensified monoclinic phase formation, further decreasing the nano-hardness and Young's modulus of the specimens. Simultaneously, increased temperature and acid concentrations contributed to larger pore sizes, which in turn led to a progressive decline in surface hardness and Young's modulus as pore size expanded. Furthermore, the incorporation of phosphate ions reduced stiffness and hardness in both groups. Notably, compared to the SS-ZrP-YSZ groups, the ZrP-YSZ groups exhibited lower nano-hardness and Young's modulus, endowing it with superior damping properties [47].

Deng et al. engineered a titanium nanotube-chitosan composite implant surface, achieving cancellous bone-matching mechanical properties (tan $\delta \approx 0.053$) through nanoscale structural optimization [25]. Inspired by periodontal ligaments, Madeira et al. fabricated porcelain-matrix composites and CoCrMo-porcelain composites with enhanced damping capacities, demonstrating loss factors of 0.024 and 0.048 respectively, while maintaining Young's modulus around 90 GPa and 140 GPa [26,48]. Although the nano-hardness and Young's modulus of ZrP-YSZ and SS-ZrP-YSZ groups differ significantly from those of cancellous bone, they approach the values found in composite ceramics, with a maximum tan $\delta \approx 0.041$ comparable to biomimetic artificial ligaments. Crucially, the bioinspired ZrP nanonetwork with large pore sizes achieved concurrent optimization of energy dissipation properties and hydrophilicity while maintaining the compactness and flexural strength of the YSZ substrate. Despite its lower tan δ compared to that of PDL *in vivo* (0.07–0.13), ZrP nanonetwork reminded us of improving energy-dissipation capability of dental ceramic prothesis by developing compressible composite structure further [49].

Interfacial bonding force critically governs the long-term stability and clinical performance of coated dental ceramics. Nanoscratch tests were used to further assess the bonding force between ZrP nanonetworks (160°C(1.0%), 160°C(2.5%), SS-160°C(1.0%), and SS-160°C(2.5%) groups) and YSZ substrate, with critical load (Lc) at coating failure marked by red boxes (Fig. S7, Supporting Information). The 160°C (1.0%) and160°C(2.5%) groups exhibited poor interfacial bonding forces (Lc < 30 mN). In contrast, SS-160°C(1.0%) and SS-160°C(2.5%) groups achieved significantly higher Lc values of 107.0 ± 2.1 mN and 97.8 ± 1.5 mN respectively, demonstrating enhanced interfacial bonding forces. This divergence originates from higher monoclinic phase content in 160°C(1.0%) and160°C(2.5%) groups promoting coating grain spalling and intergranular fracture, while the second sintering process facilitated elemental interdiffusion between ZrP nanonetworks and YSZ substrates, with increased tetragonal phase content inducing nanonetwork densification to improve debonding resistance [50].

3.2. *Application of trabecular-honeycomb ZrP nanonetwork for dental restoration*

Following the International Organization for Standardization (ISO)/TS 10477:2018 guidelines, we assessed the bonding performance between porcelain veneer and ZrP nanonetwork modified YSZ using the shear bonding strength (SBS) test. Fig. 4a illustrates the SBS test schematic. All ZrP-YSZ groups exhibited significantly higher shear stresses

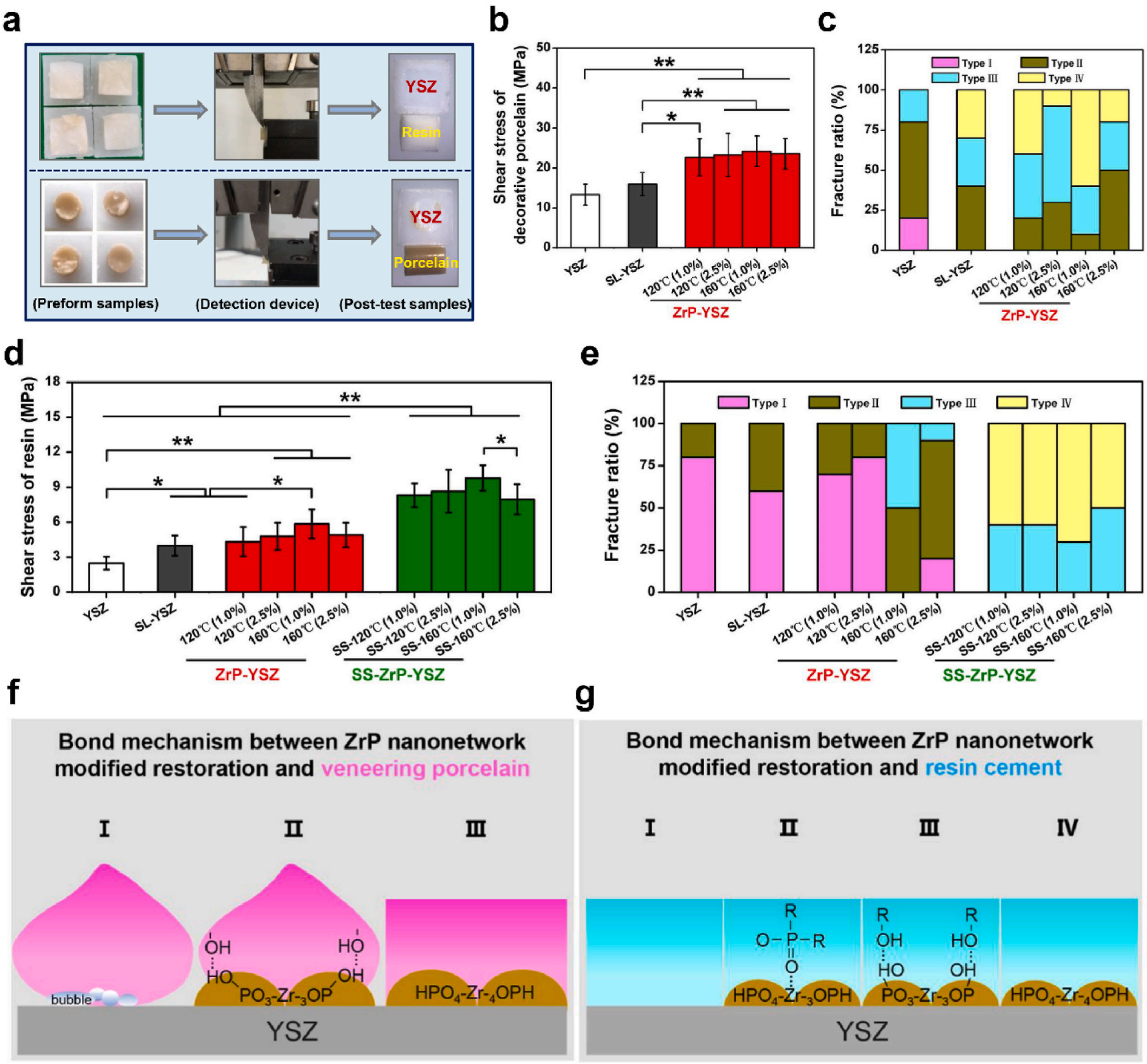

Fig. 4. The bonding performance between YSZ-based restoration and porcelain veneer as well as resin cement. a) A schematic of shear bonding strength test. b) Shear stress and c) fracture mode ratio between YSZ-based samples and porcelain veneer of each group. d) Shear stress and e) fracture mode ratio between YSZ-based samples and resin cement of each group. f) The scheme of bond mechanism between ZrP-YSZ and porcelain veneer which mainly compose of three parts: bubble defects on YSZ surface (I), the improved wettability (II) and micromechanical anchoring (III). g) The scheme of bond mechanism between ZrP-YSZ and resin cement mainly composes of four parts: chemical and physical defects on YSZ surface (I), inner-sphere complexation (II), the hydrogen-bond interaction (III), and micromechanical retention (IV). The error bars represent as mean ± SD (n = 5 samples per group). $*p < 0.05$ represents a significant difference among groups. [Abbreviations: YSZ, yttria stabilized zirconia; SL-YSZ, sandblast the surface of YSZ; ZrP-YSZ, ZrP nanonetwork modified YSZ including 120°C(1.0%), 120°C(2.5%), 160°C(1.0%) and 160°C(2.5%) groups; SS-ZrP-YSZ, second-sintered ZrP nanonetwork modified YSZ including SS-120°C(1.0%), SS-120°C(2.5%), SS-160°C(1.0%) and SS-160°C(2.5%) groups.].

(22.7–24.2 MPa) compared to YSZ (13.3 ± 2.6 MPa) and SL-YSZ (15.9 ± 2.8 MPa), as shown in shear stress statistics and shear stress-displacement curves (Fig. 4b and S8a, Supporting Information). Particularly, the 160°C (1.0%) group achieved the highest shear stress of 28.0 MPa, representing a 111 % improvement over YSZ group. While no definitive standard exists for porcelain-ceramic bonding strength in all-ceramic systems, our ZrP-YSZ groups achieved superior bonding performance with the average shear strength exceeding 20 MPa, significantly surpassing textured zirconia produced via additive manufacturing (AM) that reached a maximum strength of 18.99 MPa in prior studies [51]. Fracture mode analysis classified failures into four types based on interfacial FAR.

Type I: FAR <10 % (adhesive failure)
Type II: 10 % ≤ FAR <50 % (mixed adhesive-cohesive failure)
Type III: 50 % ≤ FAR ≤90 % (predominantly cohesive failure)
Type IV: FAR >90 % (complete cohesive failure)

All ZrP-YSZ groups predominantly exhibited Type III and IV failures (Fig. 4c and S8b, Supporting Information), with the 160°C(1.0%) group showing optimal porcelain retention (>60 % Type IV fractures). Increased bonding strength shifted the dominant failure mode from mixed adhesive-cohesive failure (common in most groups) to cohesive failure within the porcelain veneer. By contrast, unmodified YSZ displayed predominantly Type I adhesive failure, correlating with its lowest shear bonding strength. This improvement correlates with enhanced YSZ surface wettability, which reduces interfacial bubbles during molding [Fig. 4f (I)] [52]. Hence, the bonding enhancement mechanism between porcelain veneer and ZrP nanonetwork is elucidated as follows (Fig. 4f): (II) The ZrP nanonetwork enhances interfacial hydrophilicity by hydroxyl group enrichment, effectively eliminating bubbles; (III) Its topological structure increases not only the specific surface area but the micromechanical anchoring at the interface [53].

We further evaluated the bond performance between resin cement and YSZ restoration using SBS test and fracture modes ratio analysis. The SS-ZrP-YSZ groups demonstrated significantly higher shear stresses (6.8–10.8 MPa) than YSZ (2.5 ± 0.5 MPa), SL-YSZ (4.0 ± 0.8 MPa) and ZrP-YSZ (3.2–7.0 MPa) groups (Fig. 4d and S9a, Supporting Information). Notably, the SS-160°C(1.0%) group achieved the maximum shear stress of 10.9 MPa, corresponding to a 336 % increase in bonding strength with resin cement relative to the YSZ group. Fracture pattern ratio and representative fracture images aligned with SBS results, with SS-ZrP-YSZ groups predominantly displaying Type IV fractures (>50 %) (Fig. 4e and S9b, Supporting Information).This performance improvement arose from the second sintering treatment, which releases residual stresses, activates surface recomposition of YSZ, and enhanced integration of the ZrP nanonetwork into YSZ substrate [54]. Fig. 4g depicted the bonding mechanism between resin cement and ZrP nanonetwork: (II) ZrP preferentially absorbs phosphate via inner-sphere complexation [55], which facilitates the chelation with organic phosphate compounds in the resin cement for enhancing the bonding strength; (III) The ZrP nanonetwork provides P-OH groups that form hydrogen bonds with the resin cement while improving wettability; (IV) High specific surface area of the ZrP nanonetwork improves micromechanical retention and wettability. Additionally, crystal phase transformation critically influences the bonding strength between YSZ and resin cement. Previous research has reported that elevated monoclinic phase content on YSZ surface induces microcrack formation and reduces mechanical strength, ultimately diminishing interfacial bonds with resin cement [56]. XRD and Raman analyses confirmed the high monoclinic phase content in ZrP-YSZ groups, which substantially impaired their bonding efficacy with resin cement. Conversely, the second sintering treatment in SS-ZrP-YSZ group not only diminished monoclinic phase levels but also enhanced m→t reverse phase transformation, thereby sealing microcracks and increasing the bonding strength with resin cement effectively.

Based on these results, we conceived that ZrP nanonetwork provided not only the damping layer to prevent ceramic prothesis from overloading and dissipate impact better, but a desirable bond interface with porcelain veneer and resin cement for improving the clinical durability of zirconia-based restorations.

3.3. *The effects of bioinspired ZrP nanonetwork on osteogenesis in vitro*

After confirming the excellent bonding strength of SS-ZrP-YSZ nanonetwork, we then select precursor osteoblasts (MC3T3-E1) to study the osteogenic effects of the SS-ZrP-YSZ nanonetwork. The initial cell adhesion, proliferation, and osteogenic differentiation are notably influenced by proteins that adsorbed onto the implant surface. Upon implantation, serum proteins bind to the implant surface, activating

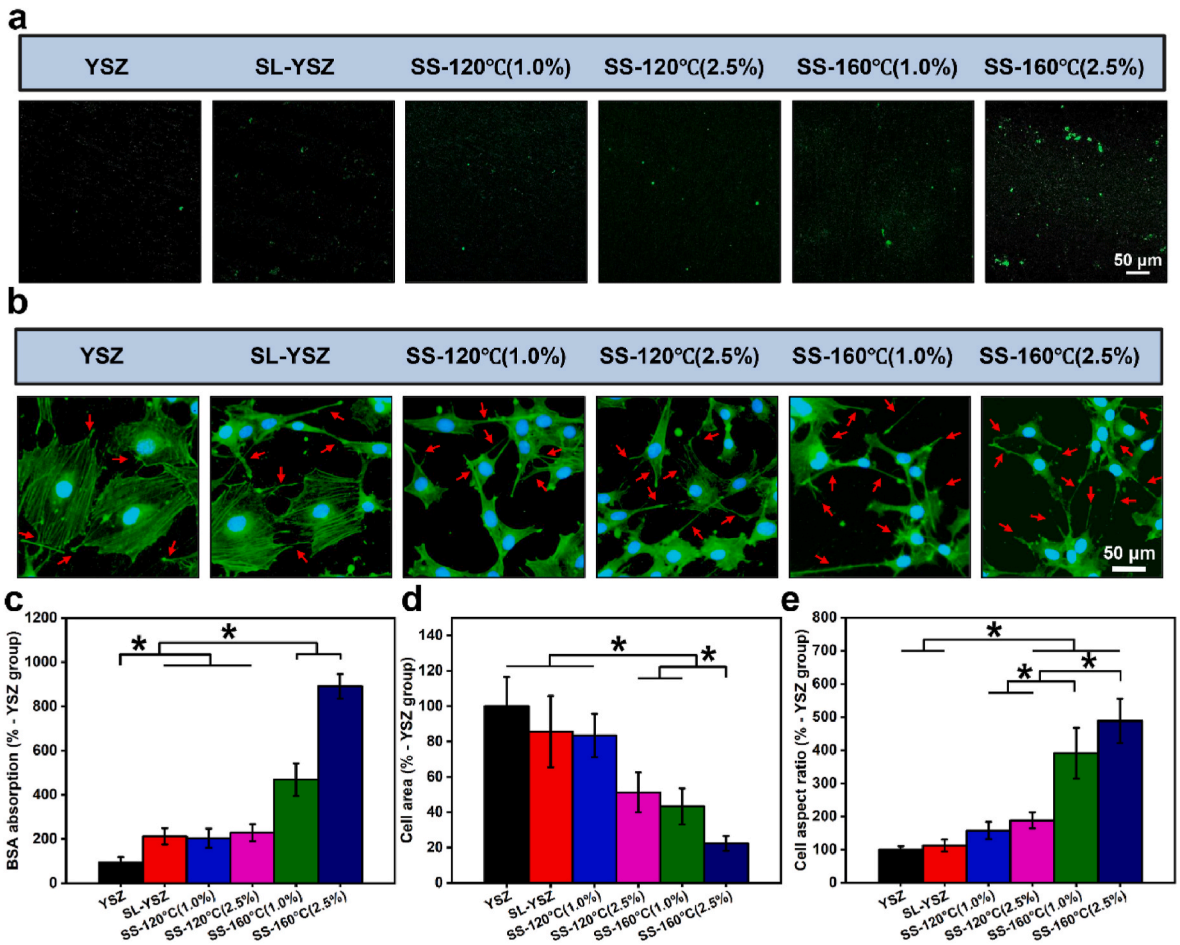

Fig. 5. The biocompatibility of SS-ZrP-YSZ nanonetwork *in vitro*. a) Representative fluorescent images of FITC-labeled BSA adsorbed on different sample surfaces at 120 min. b) Cell morphology of MC3T3-E1 cells on day 2 stained with DAPI (blue) and FITC-phalloidin (green) fluorescence, with filopodia indicated by red arrows. c) Quantitative analyses of adsorbed FITC-labeled BSA at 120 min. d) Cell area and e) cell aspect ratio of each group on day 2, which are normalized by YSZ group. The error bars represent as mean ± SD (n = 4 biological replicates). $*p < 0.05$ represents a significant difference among groups. [Abbreviations: YSZ, yttria stabilized zirconia; SL-YSZ, sandblast the surface of YSZ; SS-ZrP-YSZ, second-sintered ZrP nanonetwork modified YSZ including SS-120°C(1.0%), SS-120°C(2.5%), SS-160°C (1.0%) and SS-160°C(2.5%) groups.].

signaling pathways that modulate cellular behavior and promote bone formation [57]. To evaluate protein adsorption, FITC-labeled bovine serum albumin (BSA) was employed as a model protein. Laser confocal imaging and fluorescence quantification revealed that the SS-160°C (1.0%) and SS-160°C(2.5%) groups adsorbed significantly more BSA, with an increase of over 4-fold and 8-fold, respectively, compared to the YSZ group (Fig. 5a and c). This increased protein adsorption is attributed to the surface enrichment of ZrP and hydroxyl groups on the nanonetwork, where ZrP serves as a protein adsorbent, providing numerous binding sites. Additionally, the accumulation of protein nanoparticles is directly related to the increased specific surface area of the nanonetwork, offering an ideal environment for biocompatibility and osseointegration [34].

Changes in cell behaviors are the way osteoblasts respond to surface topological structure [58]. After co-culturing with the samples of each group for two days, noticeable alterations in cell morphology were evident through fluorescence staining of the actin cytoskeleton (labeled with FITC-phalloidin, green) and cell nucleus (labeled with DAPI, blue). MC3T3-E1 cells exhibited distinct morphological responses to surface topographies, as shown in Fig. 5b. Cells on YSZ and SL-YSZ displayed spread morphologies, whereas SS-ZrP-YSZ substrates induced progressive cytoskeletal reorganization from round shapes to spindle cell morphologies as pore size increased. Compared with the YSZ control, normalized cell spreading area decreased as pore sizes of nanonetworks increased, reaching its lowest value of 22.4 ± 4.2 % in the large-pore group. Conversely, normalized cell aspect ratio rose in parallel, peaking at 488.7 ± 66.5 % in the large-pore group (Fig. 5d and e). The rectangular morphology resulting from cell elongation is considered the initial step of osteogenic differentiation. Previous studies on titanium nanotubes topologies have shown that osteoblasts exhibit the highest elongation rate on tubes with a diameter of 150 nm, which is attributed to the enhanced interaction of filamentous pseudopods of osteoblasts with fibronectin and albumin [58]. Interestingly, our findings revealed that the greatest cell elongation rate occurred on the large-pore-size ZrP nanonetwork with a pore size of approximately 600 nm. This may be attributed to its unique trabecular-honeycomb structure of the

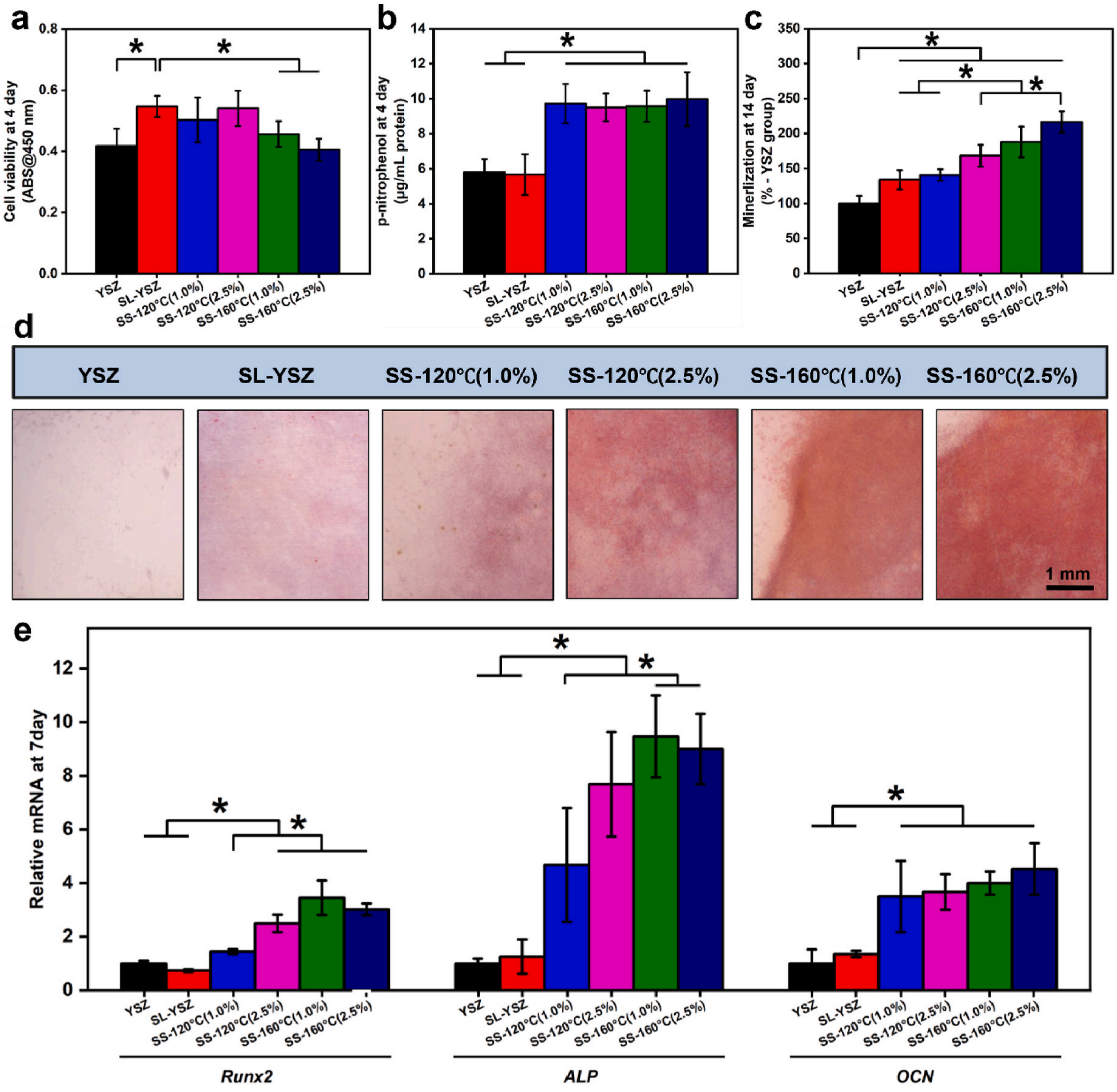

Fig. 6. The osteogenic behavior guided by SS-ZrP-YSZ nanonetwork *in vitro*. Statistics of a) cell viability and b) ALP activity of YSZ, SL-YSZ, and SS-ZrP-YSZ on day 4. c) Statistics of mineralization and d) representative alizarin red S staining photographs of different groups on day 14. e) The relative mRNA expression levels of *Runx2*, *ALP*, *OCN* genes in MC3T3-E1 cells on different groups, which are normalized by YSZ group. The error bars represent as mean ± SD (n = 4 biological replicates). *$p < 0.05$ represents a significant difference among groups. [Abbreviations: YSZ, yttria stabilized zirconia; SL-YSZ, sandblast the surface of YSZ; SS-ZrP-YSZ, second-sintered ZrP nanonetwork modified YSZ including SS-120°C(1.0%), SS-120°C(2.5%), SS-160°C(1.0%) and SS-160°C(2.5%) groups.].

nanonetwork, which potentially offers an optimal environment for medium flow. Additionally, compared to the YSZ and SL-YSZ groups, the SS-ZrP-YSZ groups exhibited more pronounced filopodia formation and greater extension lengths in osteoblasts (indicated by red arrows). Cellular filopodia regulate cell adhesion and migration by mechanosensing surface microenvironments. The pore sizes in the medium- and large-pore groups, being comparable to filopodial dimensions, provide favorable topographic cues for directed cell anchoring during the early adhesion phase [59]. Furthermore, the increased surface roughness and lower Young's modulus of the SS-160°C(2.5%) group facilitate improved cell-material interactions, further promoting filopodial extension and elongated cell morphologies [60]. Collectively, these results suggest that the nanotopological structure of ZrP network plays a crucial role in regulating osteoblast morphology.

The process of osteogenic differentiation is segmented into three primary phases: early proliferation, osteogenic differentiation, and late mineralization. The initial stage is mainly characterized by cell proliferation within the first 4 days. Subsequently, from day 4 to day 14, the differentiation process enters the early phase. This stage is marked by the MC3T3 cell line differentiation, hallmarked by intracellular ALP synthesis and the establishment of an initial extracellular matrix [61]. To assess MC3T3-E1 cell viabilities on different groups, we performed cell counting kit-8 (CCK-8) assays (Fig. 6a and S10a, Supporting Information). At day 1, the medium-pore [SS-120°C(2.5%) and SS-160°C (1.0%)] and large-pore SS-160°C(2.5%) groups exhibited significantly higher cell viability than YSZ and SL-YSZ groups, likely due to enhanced protein adsorption on their nanonetwork surfaces. By day 4, the SL-YSZ group showed a marked increase in osteoblast viability compared to the YSZ, SS-160°C(1.0%), and SS-160°C(2.5%) groups, attributed to sandblasting-induced microscale surface features favoring cell adhesion and proliferation [62]. In contrast, the medium- and large-pore nanonetworks displayed reduced cell proliferation, possibly due to the preference of osteogenic differentiation over cell proliferation [63]. All groups achieved comparable cell viability by day 7. Consequently, all SS-ZrP-YSZ nanonetworks showed no cytotoxicity throughout the culture period, indicating excellent cytocompatibility. This enhancement in biocompatibility was attributed to the combination of ZrP-mediated biochemical signaling and nanotopographical features.

We evaluated osteogenic differentiation potential of MC3T3-E1 cells after 4-day culture using ALP activity assays. All SS-ZrP-YSZ groups induced significantly higher ALP activities in osteoblasts (Fig. 6b), indicating enhanced early-stage osteogenic differentiation. The enhanced level of ALP activity was primarily ascribed to nanotopographical features and the osteoinductive property of HPO_4^{2-} ion from the ZrP nanonetwork [64].

The mineralization of the extracellular matrix starting on day 14 represents the terminal stage of osteoblast differentiation, and the mineralized nodules serve as markers of osteoblast maturation [61]. To further evaluate the effects of ZrP nanonetworks on late-stage mineralization, ARS was carried out after 14 days of osteogenic induction. Both representative ARS-staining images and quantitative analysis of mineralized nodules demonstrated significantly enhanced mineralization in all SS-ZrP-YSZ groups compared to the YSZ control, with the large-pore group exhibiting the highest normalized nodule deposition rate at 216.5 ± 15.3 % (Fig. 6c and d). The results of the mineralization experiments highlighted the potential of SS-ZrP-YSZ nanonetworks, particularly those with large-pore-size structures, in facilitating the formation of mineralized nodules and promoting osteogenic differentiation through synergistic nanotopographical features and chemical modulation. The large-pore nanonetworks promote the elongation of osteoblast cytoskeletons by providing enhanced specific surface area, ideal surface roughness, and favorable nanotopographical cues that guide cytoskeletal reorganization, thereby supporting cell growth and osteogenic differentiation [65]. Concurrently, phosphate-rich ZrP endows the nanonetworks with stable superhydrophilicity, substantially improving interfacial bioactivity for protein adsorption and cellular adhesion [64]. Consequently, the combination of large pore-mediated mechanostimulation and phosphate-driven interfacial activation creates an osteoinductive environment that further accelerates osteogenic differentiation.

Quantitative reverse transcription-polymerase chain reaction (qRT-PCR) was used to assess the expression levels of osteogenic gene markers, including early osteogenic markers [*runt-related transcription factor 2* (*Runx2*) and *ALP*] and later mineralization markers [*osteocalcin* (*OCN*)] [66]. *Runx2*, a key transcription factor in osteogenic differentiation, is highly expressed in immature osteoblasts and plays a vital role in regulating the transcription of downstream osteogenic markers, including *ALP* and *OCN*. Together, *Runx2*, *ALP*, and *OCN* form a transcriptional network that governs the process of osteogenesis [67]. As shown in Fig. 6e, the expression levels of *Runx2*, *ALP*, and *OCN* in the SS-ZrP-YSZ groups were significantly upregulated compared to those in the YSZ and SL-YSZ groups. Notably, the expression levels of osteogenic markers *Runx2* and *ALP* in the medium-pore-size SS-160°C(1.0%) group and the large-pore-size SS-160°C(2.5%) group were increased by more than 3-fold and 9-fold, respectively, compared to the YSZ group. These findings indicate that SS-ZrP-YSZ nanonetwork exerts an osteoinductive effect during bone formation by upregulating the transcription of osteogenic-related genes. WB results further validated these findings at the protein level (Figs. S10b–d, Supporting Information). Compared to the YSZ control, medium-pore groups [SS-120°C (2.5%) and SS-160°C (1.0%)] and the large-pore SS-160°C (2.5%) group exhibited significantly upregulated Runx2 and OCN protein expression. Overall, SS-ZrP-YSZ nanonetworks featuring medium-/large-pore sizes synergistically promote osteogenic gene transcription and protein expression through bioactive phosphate groups and nanotopographical features, highlighting their potential to improve early bone regeneration and osseointegration ability in zirconia implants.

3.4. The effects of bioinspired ZrP nanonetwork on immune regulation in vitro

The immune response of macrophages around implants is critical for implant osseointegration [68]. Through its surface physicochemical properties, the implant influences the polarization of macrophages towards a pro-inflammatory M1 phenotype or a pro-healing M2 phenotype [41,69]. Fig. 7 illustrated the immune response of RAW 264.7 cells on YSZ and biomimetic SS-ZrP-YSZ nanonetwork surfaces. As shown in the fluorescence-stained images in Fig. 7a, macrophages on YSZ and SL-YSZ surfaces generally displayed a disc-like shape, whereas macrophages on the SS-ZrP-YSZ nanonetwork surfaces were activated with more prominent pseudopod extension. Notably, macrophages on the medium-pore-size groups [SS-120°C(2.5%) and SS-160°C(1.0%)] and large-pore-size group [SS-160°C(2.5%)] exhibited the elongated spindle-like morphology, which was generally considered to be the morphology of the M2 phenotype [70].

To further investigate the impact of the ZrP nanonetwork on macrophage polarization, we used flow cytometry to analyze phenotypic conversion in each group, with CD86 and CD206 serving as markers for M1 and M2 macrophages, respectively. Representative flow cytometry images and semi-quantitative analysis showed that all ZrP nanonetwork surfaces provided a microenvironment conducive to macrophage polarization toward the anti-inflammatory (M2) phenotype (Fig. 7b and c). Specifically, the percentage of $CD86^+$ cells in the SS-160°C(2.5%) group significantly decreased (from 8.19 % in the YSZ group and 7.35 % in the SL-YSZ group to 4.47 % in the SS-160°C(2.5%) group), whereas the percentage of $CD206^+$ cells markedly increased (from 5.36 % in the YSZ group and 6.92 % in the SL-YSZ group to 18.21 % in the SS-160°C(2.5%) group).

Additionally, macrophage polarization-associated protein and gene expression levels were evaluated by WB and RT-qPCR respectively. WB analysis displayed significant increased CD206 protein expression in the medium-pore [SS-120°C (2.5%) and SS-160°C (1.0%)] and large-pore [SS-160°C(2.5%)] groups compared to others (Figs. S10e–f,

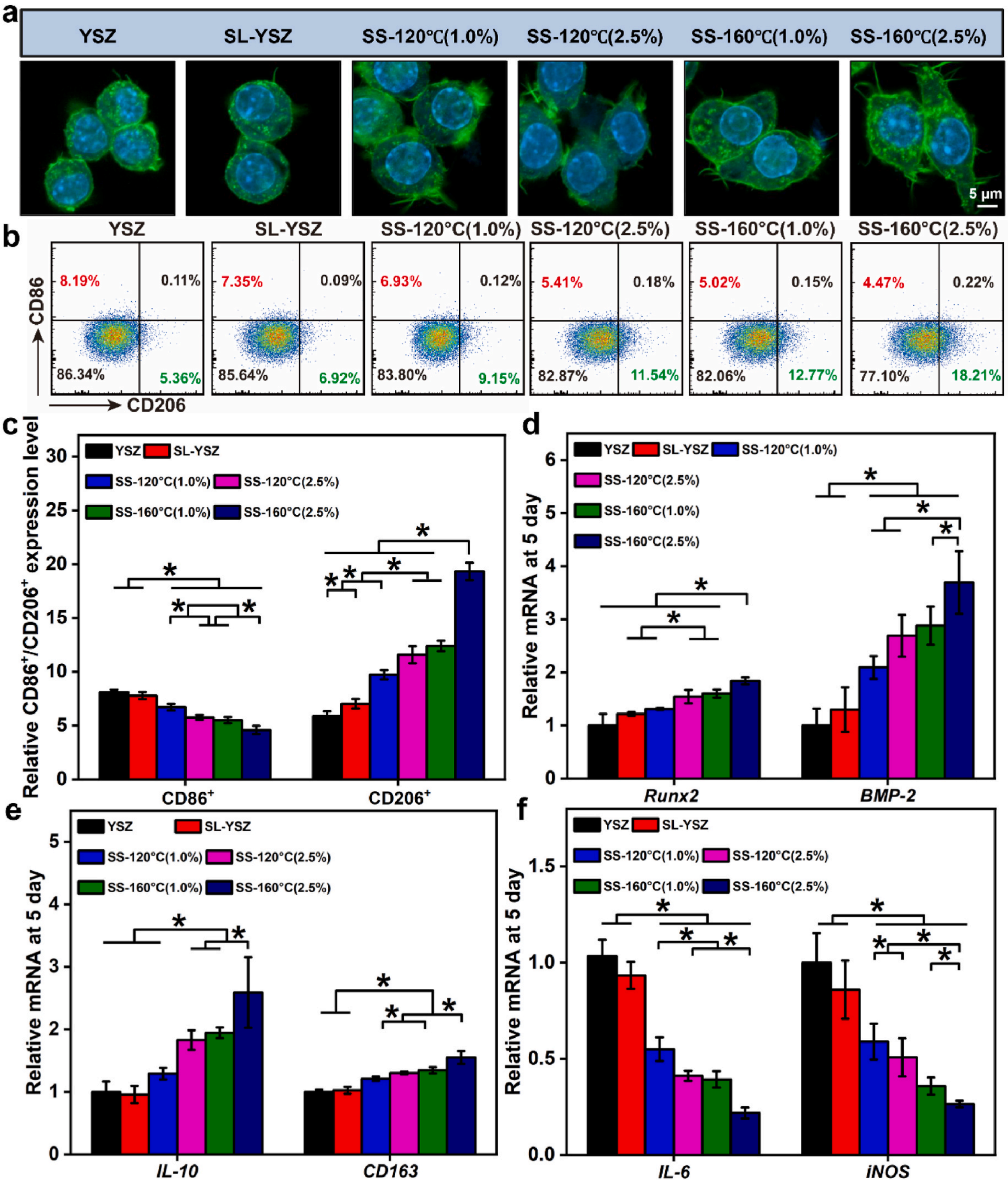

Fig. 7. The immune regulation of RAW 264.7 cells guided by SS-ZrP-YSZ nanonetwork *in vitro*. a) Cell morphology of RAW 264.7 cells stained by DAPI (blue) and FITC-phalloidin (green) fluorescence after culture for 24 h. b) Representative plots of flow cytometric analysis of macrophage surface marker (CD86/CD206). c) Quantitative analysis of CD86$^+$ (M1) and CD206$^+$ (M2) populations of macrophages on different surfaces. d-f) The relative mRNA expression levels of *Runx2*, *BMP-2*, *IL-10*, *CD163*, *IL-6* and *iNOS* genes in macrophages on different samples, which are normalized by YSZ group. The error bars represent as mean ± SD (n = 4 biological replicates). $^*p < 0.05$ represents a significant difference among groups. [Abbreviations: YSZ, yttria stabilized zirconia; SL-YSZ, sandblast the surface of YSZ; SS-ZrP-YSZ, second-sintered ZrP nanonetwork modified YSZ including SS-120°C(1.0%), SS-120°C(2.5%), SS-160°C(1.0%) and SS-160°C(2.5%) groups.].

Supporting Information), highlighting the efficacy of medium- and large-pore ZrP nanonetworks in promoting macrophage polarization toward anti-inflammatory phenotypes. RT-qPCR results in Fig. 7d–f further confirmed that the medium- and large-pore groups significantly upregulated the expression of osteogenic markers (*Runx*2 and *BMP-2*) and M2 pro-healing genes (*IL-10* and *CD163*), while significantly downregulating the expression of M1 pro-inflammatory genes (*IL-6* and *iNOS*). Notably, the large-pore SS-160°C(2.5%) group showed the most pronounced M2 polarization, with *IL-10* and *CD163* expression levels 2.6- and 1.6-fold higher, respectively, than the YSZ group. The micro-nano topological structures on implant surfaces play a crucial role in modulating macrophage-mediated immune responses. Deng et al. demonstrated that micro-nano structures with large pores reduced external stimuli, triggering the Src/ROCK pathway to upregulate ROCK expression, induce macrophage elongation and promote macrophage polarization toward M2 phenotype [71]. Zhou et al. found that larger nanotubular surfaces not only suppressed the expression of pro-inflammatory factors but also upregulated macrophage secretion of anti-inflammatory factors [72]. In addition to surface pore size, surface wettability and stiffness also critically regulate macrophage polarization behavior. Hydrophilic nanotopographic surface can induce macrophage autophagy by activating the ERK signaling pathway, while enhancing *IL-10* and *CD163* expression, thereby effectively promoting M2 polarization [73]. Furthermore, substrate stiffness also influenced the phenotypic modulation of macrophages, with lower Young's modulus materials promoting macrophage conversion toward anti-inflammatory phenotype [74]. Our findings revealed that the large-pore SS-160°C (2.5%) group, characterized by hydrophilic surface and reduced Young's modulus, significantly stimulated M2-polarized macrophages and upregulated *IL-10* and *CD163* gene expression. This shift towards an M2-dominated immune response helps the transition from a pro-inflammatory to an anti-inflammatory state, thereby promoting bone healing and remodeling.

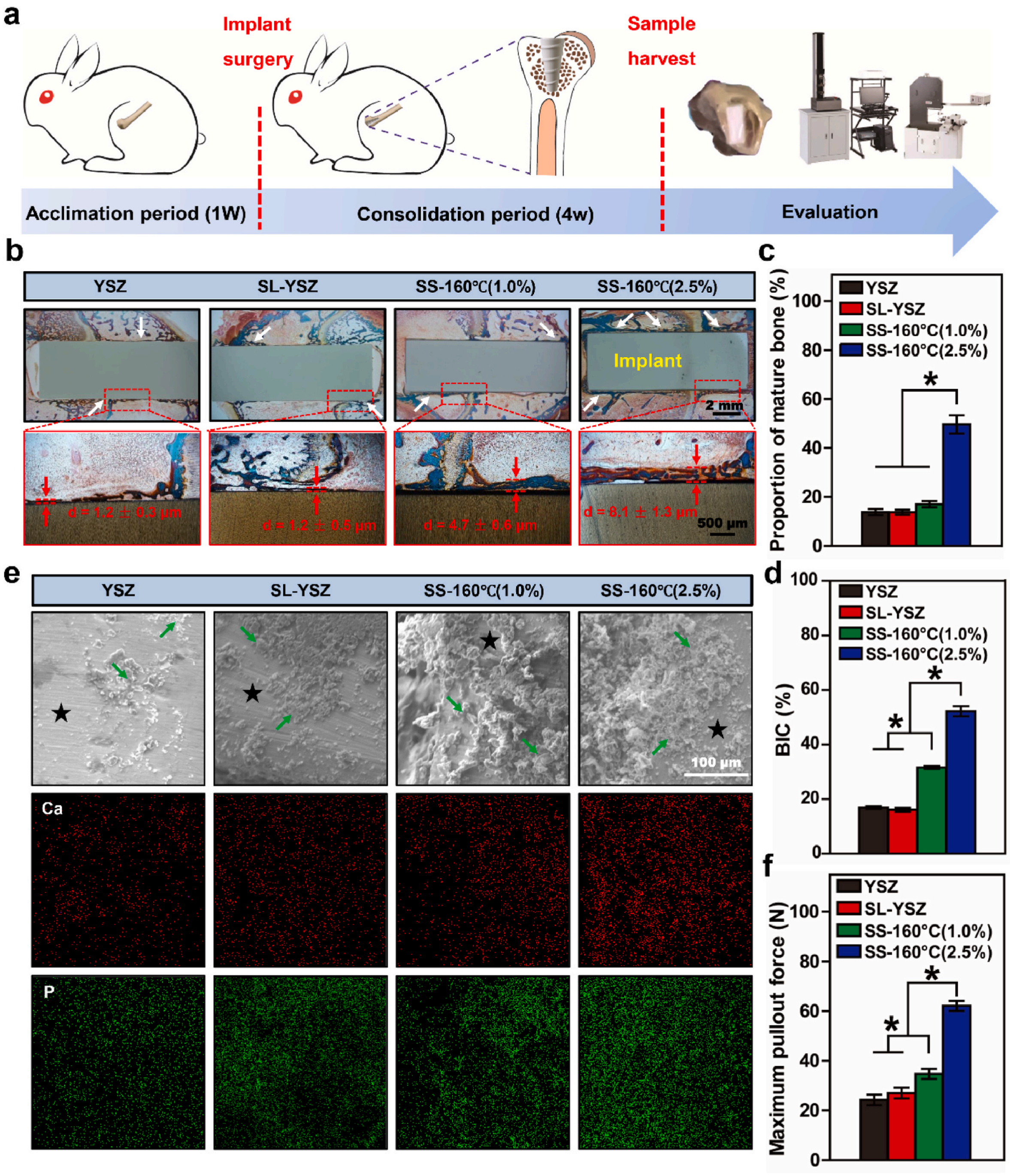

Fig. 8. Bone regeneration and osseointegration abilities of SS-ZrP-YSZ nanonetwork *in vivo*. a) Schematic diagram of the experimental protocol for *in vivo* osteogenic evaluation in the rabbit's femur implantation model. b) Representative histological images of Masson's trichrome staining (mature bone tissue appeared red staining; immature bone tissue appeared blue staining) at 12 × (upper panel) and 40 × (lower panel) magnifications. Newly formed bones are pointed by white arrows. c) Quantification of the proportion of mature bone (indicated by red staining) within the ROI around implants after 4 weeks of implantation. d) Statistics of bone-implant contact (BIC) rates within the ROI. e) Representative SEM images (implants marked with black stars; residual interfacial tissues labeled with green arrows) and EDS elemental mapping (Ca and P) of extracted implant surface tissues after the pullout test. f) Measurement of the maximum pullout force of different implant samples. The error bars represent as mean ± SD (n = 5 rabbits per group). *$p < 0.05$ represents a significant difference among groups.

3.5. The effects of bioinspired ZrP nanonetwork on bone regeneration and osseointegration *in vivo*

Based on a comprehensive consideration of surface characterization, mechanical properties, and osteoblast behaviors in the osteogenic differentiation of ZrP nanonetwork, we concluded that the medium-pore-size SS-160°C(1.0%) group and the large-pore-size SS-160°C(2.5%) group provided the most favorable geography to promote the osteogenesis *in vitro*. We further hypothesized that SS-160°C(1.0%) and SS-160°C(2.5%) groups would also accelerate bone regeneration *in vivo*. To further assess the quantity and maturity of regenerated bone around ceramic implants *in vivo*, male Japanese white rabbits were dealt with the cylindrical bone defect drilled into the medial epicondyle of femur for insertion of implants of YSZ, SL-YSZ, SS-160°C(1.0%) and SS-160°C (2.5%) groups respectively. The experimental scheme is shown in Fig. 8a. Given that the newly formed bone around the implant provides stronger bone-implant interface strength, our research focused on the fourth week post-implantation [75]. After 4 weeks of implantation, femurs with implants were harvested, sliced, and subsequently stained with Masson's trichrome stain to evaluate the formation of new bone. Representative histological images of Masson's trichrome staining (Fig. 8b) demonstrated significantly enhanced bone regeneration in the SS-160°C(1.0%) and SS-160°C(2.5%) groups, characterized by dense newly formed bone (white arrows) at the bone-implant interface. In contrast, YSZ and SL-YSZ groups exhibited sparse and limited peri-implant newly formed bone with pronounced gaps between new bone and implants. Quantitative analysis revealed that the SS-160°C (2.5%) group achieved an average new bone thickness of 8.1 μm, representing a 6.7-fold increase than control groups, confirming the superior capacity of large-pore ZrP nanonetwork to promoting new bone regeneration. The region of interest (ROI) was delineated as a cylindrical area measuring 4 mm in length and 500 μm in thickness surrounding the implant. Quantification analysis of the proportion of mature bone, as shown in Fig. 8c, revealed that the SS-160°C (1.0%) group demonstrated a slightly higher proportion of mature bone, though no statistically significant difference was observed compared to the YSZ and SL-YSZ groups. In contrast, the proportion of mature bone within the ROI of the SS-160°C (2.5%) group reached 49.58 ± 0.06 %, roughly 2.9 times higher than that of the YSZ group, highlighting the significant role of the large-pore-size structure in promoting bone maturation. Statistical analysis of the bone-implant contact (BIC) rate presented in Fig. 8d, further supported this observation. Specifically, the BIC rates for the SS-160°C (1.0%) and SS-160°C (2.5%) groups were 31.60 ± 0.82 % and 52.24 ± 3.21 %, respectively, both significantly higher than those of the YSZ group (16.91 ± 0.78 %) and the SL-YSZ group (16.11 ± 1.32 %). Notably, the BIC rate of the SS-160°C (2.5%) group was 3 times and 3.2 times higher than those of the YSZ and SL-YSZ groups, respectively, further confirming the significant impact of the large-pore-size SS-ZrP-YSZ nanonetwork in enhancing early osseointegration.

We further quantified the interface bonding strength between the implants and the newly formed bone using pullout tests. According to the pullout test results in Fig. 8f, the maximum pullout force of the SS-160°C (1.0%) group increased slightly compared to the YSZ and SL-YSZ groups. In comparison, the SS-160°C (2.5%) group exhibited a higher maximum pullout force, reaching 62.1 ± 3.36 N, which was substantially higher than the other groups. This indicated that the large-pore SS-ZrP-YSZ nanonetworks significantly enhanced the mechanical bonding strength between the implants and bone tissue. SEM observations and EDS analyses of the zirconia implant surfaces from each group following the pullout tests (Fig. 8e) showed obvious implant exposure (marked by black stars) and lower residual calcium and phosphorus (Ca/P) content (marked by green arrows) in the YSZ and SL-YSZ groups. In contrast, the failure interfaces of implants in the SS-160°C (1.0%) and SS-160°C (2.5%) groups exhibited a large amount of residual tissue and significantly elevated Ca/P content, suggesting that the failure during pullout tests predominantly occurred within the bone tissue rather than at the bone-implant contact interface. Particularly in the large-pore-size SS-160°C (2.5%) group, the implants exhibited a tighter bond with the surface residual tissues rich in Ca/P content. These findings collectively demonstrated that the large-pore-size SS-ZrP-YSZ nanonetwork plays a crucial role in inducing bone formation *in vivo*, effectively facilitating the close integration between implants and bone tissue at early stages and significantly improving osseointegration. Compared to our previous research [76], zirconia implants modified with the trabecular-honeycomb ZrP nanonetwork demonstrated significantly superior osteogenic effects *in vivo* within the first 4 weeks, surpassing those of zirconia implants modified with the nanoporous tantalum coating. This further confirmed the significant advantages of large-pore-size SS-ZrP-YSZ nanonetworks in stimulating new bone regeneration and osseointegration around zirconia implants.

Drawing from the *in vivo* results, the SS-160°C(2.5%) group effectively facilitated new bone formation, primarily driven by its surface nanotopological structure. Additionally, the active phosphate groups within the ZrP compound further enhanced the osteoinductive potential of zirconia implants. These two factors worked synergistically to enhance bone regeneration and accelerate bone maturation *in vivo*. Moreover, we believed that the ZrP nanonetwork improved the energy dispersion capacity of the zirconia surface, optimizing stress distribution between the implant and alveolar bone and reducing stress concentration [77]. This improvement further supported bone remodeling. Zirconia implants modified with the large-pore-size SS-ZrP-YSZ nanonetwork exhibited accelerated osteogenesis and osseointegration, contributing to improved long-term performance and extending the lifespan of dental implants.

4. Conclusion

In summary, enlightened by the elytra structure, we proposed a newly strategy to produce a high-bioactivity biomimetic self-assembled ZrP nanonetwork on YSZ by the hydrothermal reaction based on martensitic phase transformation and Ostwald ripening process. We found that the pore size and energy-dissipation capacity of ZrP nanonetwork were highly controlled by reaction temperatures (120 °C and 160 °C) and H_3PO_4 concentrations (1.0 wt% and 2.5 wt%). Higher temperatures and H_3PO_4 concentrations lead to increased generation of Zr^{4+} ions, which further enhance the dynamic dissolution and re-precipitation of ZrP under the Ostwald ripening mechanism, resulting in the formation of the self-assembled ZrP nanonetwork with large pore size and high energy-dissipation capacity. The nanostructures and active phosphate groups of second-sintered ZrP nanonetworks not only ensure high-quality bonding between the interface of nanonetwork and porcelain veneer/resin cement but also establish an anti-inflammatory microenvironment and facilitate osteogenic differentiation of osteoblasts *in vitro*. Particularly, it is worth stressing that the SS-160°C(2.5%) group with large pore size exhibits higher bonding strength and superior bone-forming capacity, in addition to facilitating the polarization of macrophages to the anti-inflammatory M2 phenotype. Moreover, the implantation experiment in rabbit femurs demonstrated that the large-pore-size SS-160°C (2.5%) group markedly improved early osseointegration and new bone regeneration, achieving a new bone maturation rate of 49.58 ± 0.06 % and a BIC rate of 52.24 ± 3.21 %. To conclude, this research offers an efficient approach to creating high-bioactivity energy-dissipative interfaces on zirconia-based materials, successfully addressing the limitations of conventional zirconia-based dental materials in terms of poor osseointegration and weak bonding quality. Consequently, we anticipate that zirconia-based implants and prostheses modified with ZrP nanonetworks possess significant potential for advanced medical applications.

CRediT authorship contribution statement

Shuyi Wu: Writing – original draft, Methodology, Conceptualization. **Yingyue Sun:** Writing – original draft, Formal analysis. **Qihong Zhang:** Validation, Investigation. **Wen Si:** Data curation. **Peng Gao:** Investigation. **Lei Lu:** Investigation. **Zhennan Deng:** Formal analysis. **Lihua Xu:** Supervision, Methodology. **Xinkun Shen:** Writing – review & editing, Resources. **Jinsong Liu:** Writing – review & editing, Resources, Project administration, Conceptualization.

Ethics approval and consent to participate

All animal experiments carried out in the Animal Experiment Center of Wenzhou Institute of Biomaterials and Engineering were approved by the Animal Ethics Committee of Wenzhou Institute University of Chinese Academy of Sciences (Approval number: WIUCAS22111001) and strictly followed the ethical and welfare requirements of the Animal Experiment Center of Wenzhou Institute of Biomaterials and Engineering during experiments.

Declaration of competing interest

The authors declare no interest conflict. The authors declare that they have no known competing financial interests or personal relationships that could have appeared to influence the work reported in this paper.

Acknowledgments

This work was funded by the National Natural Science Foundation of China (No. 82071170, No. 82371016, No. 82301156, and No. 82171004), Key Technological Innovation Projects of Wenzhou (ZY2019009), Wenzhou Major Scientific and Technological Innovation Project (ZZN2023001), and Wenzhou Public Welfare Science and Technology Project (Y20210114).

Appendix A. Supplementary data

Supplementary data to this article can be found online at https://doi.org/10.1016/j.bioactmat.2025.03.028.

References

[1] S. Roehling, K.A. Schlegel, H. Woelfler, M. Gahlert, Zirconia compared to titanium dental implants in preclinical studies-A systematic review and meta-analysis, Clin. Oral Implants Res. 30 (5) (2019) 365–395, https://doi.org/10.1111/clr.13425.

[2] K. Sivaraman, A. Chopra, A.I. Narayan, D. Balakrishnan, Is zirconia a viable alternative to titanium for oral implant? A critical review, J. Prosthodont. Res. 62 (2) (2018) 121–133, https://doi.org/10.1016/j.jpor.2017.07.003.

[3] B. Stadlinger, M. Hennig, U. Eckelt, E. Kuhlisch, R. Mai, Comparison of zirconia and titanium implants after a short healing period. A pilot study in minipigs, Int J Oral Max Surg 39 (6) (2010) 585–592, https://doi.org/10.1016/j.ijom.2010.01.015.

[4] C.J. Frandsen, K. Noh, K.S. Brammer, G. Johnston, S. Jin, Hybrid micro/nano-topography of a TiO2 nanotube-coated commercial zirconia femoral knee implant promotes bone cell adhesion in vitro, Mater. Sci. Eng. C. Mater. Biol. Appl. 33 (5) (2013) 2752–2756, https://doi.org/10.1016/j.msec.2013.02.045.

[5] T. Miyazaki, T. Nakamura, H. Matsumura, S. Ban, T. Kobayashi, Current status of zirconia restoration, J. Prosthodont. Res. 57 (4) (2013) 236–261, https://doi.org/10.1016/j.jpor.2013.09.001.

[6] A. Kocjan, A. Abram, A. Dakskobler, Impact strengthening of 3Y-TZP dental ceramic root posts, J. Eur. Ceram. Soc. 40 (14) (2020) 4765–4773, https://doi.org/10.1016/j.jeurceramsoc.2020.02.040.

[7] A. Casucci, E. Osorio, R. Osorio, F. Monticelli, M. Toledano, C. Mazzitelli, M. Ferrari, Influence of different surface treatments on surface zirconia frameworks, J. Dent. 37 (11) (2009) 891–897, https://doi.org/10.1016/j.jdent.2009.06.013.

[8] A.F. Han, J.K.H. Tsoi, J.P. Matinlinna, Y. Zhang, Z.F. Chen, Effects of different sterilization methods on surface characteristics and biofilm formation on zirconia in vitro, Dent. Mater. 34 (2) (2018) 272–281, https://doi.org/10.1016/j.dental.7017.11.017.

[9] A. Moradabadi, S.E. Roudsari, B.E. Yekta, N. Rahbar, Effects of surface treatment on bond strength between dental resin agent and zirconia ceramic, Mater. Sci. Eng. C. Mater. Biol. Appl. 34 (2014) 311–317, https://doi.org/10.1016/j.msec.2013.09.015.

[10] Y. Zhang, B.R. Lawn, E.D. Rekow, V.P. Thompson, Effect of sandblasting on the long-term performance of dental ceramics, J. Biomed. Mater. Res. B Appl. Biomater. 71 (2) (2004) 381–386, https://doi.org/10.1002/jbm.b.30097.

[11] G. Soon, B. Pingguan-Murphy, K.W. Lai, S.A. Akbar, Review of zirconia-based bioceramic: surface modification and cellular response, Ceram. Int. 42 (11) (2016) 12543–12555, https://doi.org/10.1016/j.ceramint.2016.05.077.

[12] S.Q. Guo, N. Liu, K. Liu, Y. Li, W. Zhang, B. Zhu, B. Gu, N. Wen, Effects of carbon and nitrogen plasma immersion ion implantation on bioactivity of zirconia, Rsc. Adv. 10 (59) (2020) 35917–35929, https://doi.org/10.1039/d0ra05853j.

[13] A.O. Abdullah, F.K. Muhammed, H. Yu, S. Pollington, S. Xudong, Y. Liu, The impact of laser scanning on zirconia coating and shear bond strength using veneer ceramic material, Dent. Mater. J. 38 (3) (2019) 452–463, https://doi.org/10.4012/dmj.2018-091.

[14] B. Henriques, N. Hammes, J.C.M. Souza, M. Ozcan, J. Mesquita-Guimaraes, F. S. Silva, M.C. Fredel, C.M. Volpato, O. Carvalho, Influence of Ns-Nd:YAG laser surface treatment on the tensile bond strength of zirconia to resin-matrix cements, Ceram. Int. 46 (17) (2020) 27822–27831, https://doi.org/10.1016/j.ceramint.2020.07.281.

[15] J. Minguela, D.W. Muller, F. Mucklich, L. Llanes, M.P. Ginebra, J.J. Roa, C. Mas-Moruno, Peptidic biofunctionalization of laser patterned dental zirconia: a biochemical-topographical approach, Mater. Sci. Eng. C. Mater. Biol. Appl. 125 (2021) 112096, https://doi.org/10.1016/j.msec.2021.112096.

[16] Z. Huang, Z. Wang, C. Li, N. Zhou, F. Liu, J. Lan, The osteoinduction of RGD and Mg ion functionalized bioactive zirconia coating, J. Mater. Sci. Mater. Med. 30 (8) (2019) 95, https://doi.org/10.1007/s10856-019-6298-7.

[17] S.K. Hsu, P.L. Chang, W.F. Ho, H.C. Hsu, H.J. Liao, S.C. Wu, Osteogenesis ability of biomimetic modified 3Y-TZP ceramic using chemical treatment, Thin Solid Films 596 (2015) 118–127, https://doi.org/10.1016/j.tsf.2015.09.079.

[18] E. Roitero, F. Lasserre, M. Anglada, F. Mucklich, E. Jimenez-Pique, A parametric study of laser interference surface patterning of dental zirconia: effects of laser parameters on topography and surface quality, Dent. Mater. 33 (1) (2017) E28–E38, https://doi.org/10.1016/j.dental.2016.09.040.

[19] A. Valian, E. Moravej-Salehi, Surface treatment of feldspathic porcelain: scanning electron microscopy analysis, J. Adv. Prosthodont. 6 (5) (2014) 387–394, https://doi.org/10.4047/jap.2014.6.5.387.

[20] J.W. Xiang, J.X. Du, Energy absorption characteristics of bio-inspired honeycomb structure under axial impact loading, Mater. Sci. Eng. A-Struct. Mater. Prop. Microstruct. Process. 696 (2017) 283–289, https://doi.org/10.1016/j.msea.2017.04.044.

[21] S.E. Naleway, M.M. Porter, J. McKittrick, M.A. Meyers, Structural design elements in biological materials: application to bioinspiration, Adv. Mater. 27 (37) (2015) 5455–5476, https://doi.org/10.1002/adma.201502403.

[22] Q.C. Zhang, X.H. Yang, P. Li, G.Y. Huang, S.S. Feng, C. Shen, B. Han, X.H. Zhang, F. Jin, F. Xu, T.J. Lu, Bioinspired engineering of honeycomb structure - using nature to inspire human innovation, Prog. Mater. Sci. 74 (2015) 332–400, https://doi.org/10.1016/j.pmatsci.2015.05.001.

[23] J.X. Du, P. Hao, M.B. Liu, F. Scarpa, Multi-cell energy-absorbing structures with hollow columns inspired by the beetle elytra, J. Mater. Sci. 55 (10) (2020) 4279–4291, https://doi.org/10.1007/s10853-019-04190-4.

[24] A. Nikolaus, J.D. Currey, T. Lindtner, C. Fleck, P. Zaslansky, Importance of the variable periodontal ligament geometry for whole tooth mechanical function: a validated numerical study, J. Mech. Behav. Biomed. Mater. 67 (2017) 61–73, https://doi.org/10.1016/j.jmbbm.2016.11.020.

[25] J. Hou, Z. Xiao, Z. Liu, H. Zhao, Y. Zhu, L. Guo, Z. Zhang, R.O. Ritchie, Y. Wei, X. Deng, An amorphous peri-implant ligament with combined osteointegration and energy-dissipation, Adv. Mater. 33 (45) (2021) e2103727, https://doi.org/10.1002/adma.202103727.

[26] S. Madeira, M. Gasik, J.C.M. Souza, F.S. Silva, B. Henriques, Damping and mechanical behavior of metal-ceramic composites applied to novel dental restorative systems, J. Mech. Behav. Biomed. Mater. 90 (2019) 239–247, https://doi.org/10.1016/j.jmbbm.2018.09.046.

[27] J. Guo, Stress design of the ceramic grain boundary, Mater. Chem. Phys. 43 (2) (1996) 99–102, https://doi.org/10.1016/0254-0584(96)01612-4.

[28] H.M. Ansari, V. Dixit, L.B. Zimmerman, M.D. Rauscher, S.A. Dregia, S.A. Akbar, Self assembly of nanoislands on YSZ-(001) surface: a mechanistic approach toward a robust process, Nano Lett. 13 (5) (2013) 2116–2121, https://doi.org/10.1021/nl4005282.

[29] H. Zhou, S. Pu, J. Huo, W. Cao, B. Wang, J. Li, Facile corrosion synthesis and sintering of disperse pure tetragonal zirconia nanoparticles, Ceram. Int. 42 (13) (2016) 15005–15011, https://doi.org/10.1016/j.ceramint.2016.06.148.

[30] W. Janusz, V. Sydorchuk, E. Skwarek, S. Khalameida, Effect of hydrothermal treatment of hydrogel zirconium phosphate on its surface groups properties, J. Mol. Liq. 340 (2021) 117154, https://doi.org/10.1016/j.molliq.2021.117154.

[31] H.R. Chen, J.L. Shi, Z.L. Hua, M.L. Ruan, D.S. Yan, Parameter control in the synthesis of ordered porous zirconium oxide, Mater. Lett. 51 (3) (2001) 187–193, https://doi.org/10.1016/s0167-577x(01)00286-5.

[32] S.N. Pavlova, V.A. Sadykov, G.V. Zabolotnaya, R.I. Maximovskaya, V.I. Zaikovskii, S.V. Tsybulya, E.B. Burgina, M.V. Chaikina, D. Agrawal, R. Roy, The influence of solid precursors nature on structural, textural and surface properties of framework zirconium phosphates synthesized via mechanochemical activation, Solid State Ionics 141 (2001) 683–688, https://doi.org/10.1016/s0167-2738(01)00778-0.

[33] G. Pezzotti, A.A. Porporati, Raman spectroscopic analysis of phase-transformation and stress patterns in zirconia hip joints, J. Biomed. Opt. 9 (2) (2004) 372–384, https://doi.org/10.1117/1.1647547.

[34] D. Xie, C. Xu, C. Ye, S. Mei, L. Wang, Q. Zhu, Q. Chen, Q. Zhao, Z. Xu, J. Wei, L. Yang, Fabrication of submicro-nano structures on polyetheretherketone surface

by femtosecond laser for exciting cellular responses of MC3T3-E1 cells/gingival epithelial cells, Int. J. Nanomed. 16 (2021) 3201–3216, https://doi.org/10.2147/IJN.S303411.

[35] L. Zhang, X. Shi, S. Liu, V.K. Pareek, J. Liu, Organic-inorganic hybrid hierarchical aluminum phenylphosphonate microspheres, J. Colloid Interface Sci. 427 (2014) 35–41, https://doi.org/10.1016/j.jcis.2014.04.008.

[36] S. Deville, J. Chevalier, L. Gremillard, Influence of surface finish and residual stresses on the ageing sensitivity of biomedical grade zirconia, Biomaterials 27 (10) (2006) 2186–2192, https://doi.org/10.1016/j.biomaterials.2005.11.021.

[37] S. Deville, G. Guenin, J. Chevalier, Martensitic transformation in zirconia - Part II. Martensite growth, Acta Mater. 52 (19) (2004) 5709–5721, https://doi.org/10.1016/j.actamat.2004.08.036.

[38] M. Shuai, A.F. Mejia, Y.W. Chang, Z.D. Cheng, Hydrothermal synthesis of layered alpha-zirconium phosphate disks: control of aspect ratio and polydispersity for nano-architecture, Crystengcomm 15 (10) (2013) 1970–1977, https://doi.org/10.1039/c2ce26402a.

[39] N. Benna, N. Kbir-Ariguib, C. Clinard, F. Bergaya, Card-house microstructure of purified sodium montmorillonite gels evidenced by filtration properties at different pH. 3rd International Conference of the Kolloid-Gesellschaft, 2000, pp. 204–210. Budapest, Hungary.

[40] K. Mitsuhashi, N. Tagami, K. Tanabe, T. Ohkubo, H. Sakai, M. Koishi, M. Abe, Synthesis of microtubes with a surface of "house of cards" structure via needlelike particles and control of their pore size, Langmuir 21 (8) (2005) 3659–3663, https://doi.org/10.1021/la047580o.

[41] L. Bai, P. Chen, Y. Zhao, R. Hang, X. Yao, B. Tang, C. Liu, Y. Xiao, R. Hang, A micro/nano-biomimetic coating on titanium orchestrates osteo/angio-genesis and osteoimmunomodulation for advanced osseointegration, Biomaterials 278 (2021) 121162, https://doi.org/10.1016/j.biomaterials.2021.121162.

[42] F.F. Lange, G.L. Dunlop, B.I. Davis, Degradation during aging of transformation-toughened ZrO_2-Y_2O_3 materials at 250°C, J. Am. Ceram. Soc. 69 (3) (1986) 237–240, https://doi.org/10.1111/j.1151-2916.1986.tb07415.x.

[43] D.J. Green, A technique for introducing surface compression into zirconia ceramics, J. Am. Ceram. Soc. 66 (10) (1983) C178–C179, https://doi.org/10.1111/j.1151-2916.1983.tb10543.x.

[44] S. Wille, P. Zumstrull, V. Kaidas, L.K. Jessen, M. Kern, Low temperature degradation of single layers of multilayered zirconia in comparison to conventional unshaded zirconia: phase transformation and flexural strength, J. Mech. Behav. Biomed. Mater. 77 (2018) 171–175, https://doi.org/10.1016/j.jmbbm.2017.09.010.

[45] G. Roebben, B. Basu, J. Vleugels, O. Van der Biest, Transformation-induced damping behaviour of Y-TZP zirconia ceramics, J. Eur. Ceram. Soc. 23 (3) (2003) 481–489, https://doi.org/10.1016/s0955-2219(02)00101-2.

[46] S.A. Catledge, M. Cook, Y.K. Vohra, E.M. Santos, M.D. McClenny, K. David Moore, Surface crystalline phases and nanoindentation hardness of explanted zirconia femoral heads, J Mater Sci Mater M 14 (10) (2003) 863–867, https://doi.org/10.1023/a:1025678525474.

[47] L. Vojkuvka, A. Santos, J. Pallares, J. Ferre-Borrull, L.F. Marsal, J.P. Celis, On the mechanical properties of nanoporous anodized alumina by nanoindentation and sliding tests, Surf. Coat. Tech. 206 (8–9) (2012) 2115–2124, https://doi.org/10.1016/j.surfcoat.2011.09.040.

[48] S. Madeira, J. Mesquita-Guimaraes, P. Ribeiro, M. Fredel, J.C.M. Souza, D. Soares, F.S. Silva, B. Henriques, Y-TZP/porcelain graded dental restorations design for improved damping behavior - a study on damping capacity and dynamic Young's modulus, J. Mech. Behav. Biomed. Mater. 96 (2019) 219–226, https://doi.org/10.1016/j.jmbbm.2019.04.033.

[49] P. Magne, M. Silva, E. Oderich, L.L. Boff, R. Enciso, Damping behavior of implant-supported restorations, Clin. Oral. Implan. Res. 24 (2) (2013) 143–148, https://doi.org/10.1111/j.1600-0501.2011.02311.x.

[50] J.J. Roa, M. Anglada, Annealing aged zirconia: study of surface mechanical properties at the micrometric length scale, J. Eur. Ceram. Soc. 35 (3) (2015) 1031–1039, https://doi.org/10.1016/j.jeurceramsoc.2014.10.023.

[51] K. Dai, J. Wu, Z. Zhao, H. Yu, Z. Zhao, B. Gao, Surface texture designs to improve the core-veneer bond strength of zirconia restorations using digital light processing, Materials 16 (18) (2023) 6072, https://doi.org/10.3390/ma16186072.

[52] T.Y. Peng, S. Shimoe, L.J. Fuh, C.K. Lin, D.J. Lin, M. Kaku, Bonding and thermal cycling performances of two (poly)aryl-ether-ketone (PAEKs) materials to an acrylic denture base resin, Polymers 13 (4) (2021), https://doi.org/10.3390/polym13040543. Article 543.

[53] A. Madani, M. Nakhaei, P. Karami, G. Rajabzadeh, S. Salehi, H. Bagheri, Sol-gel dip coating of yttria-stabilized tetragonal zirconia dental ceramic by aluminosilicate nanocomposite as a novel technique to improve the bonding of veneering porcelain, Int. J. Nanomed. 11 (2016) 3215–3223, https://doi.org/10.2147/IJN.S104885.

[54] J.R. Queiroz, P. Benetti, M. Massi, L.N. Junior, A. Della Bona, Effect of multiple firing and silica deposition on the zirconia-porcelain interfacial bond strength, Dent. Mater. 28 (7) (2012) 763–768, https://doi.org/10.1016/j.dental.2012.03.014.

[55] Q.R. Zhang, Q. Du, T.F. Jiao, B.C. Pan, Z.X. Zhang, Q.N. Sun, S.F. Wang, T. Wang, F.M. Gao, Selective removal of phosphate in waters using a novel of cation adsorbent: zirconium phosphate (ZrP) behavior and mechanism, Chem. Eng. J. 221 (2013) 315–321, https://doi.org/10.1016/j.cej.2013.02.001.

[56] G.E. You, M.J. Lim, K.S. Min, M.K. Yu, K.W. Lee, Surface property changes observed in zirconia during etching with high-concentration hydrofluoric acid over various immersion times, Dent. Mater. J. 43 (1) (2024) 52–57, https://doi.org/10.4012/dmj.2023-091.

[57] F. Deng, W. Zhai, Y. Yin, C. Peng, C. Ning, Advanced protein adsorption properties of a novel silicate-based bioceramic: a proteomic analysis, Bioact. Mater. 6 (1) (2021) 208–218, https://doi.org/10.1016/j.bioactmat.2020.08.011.

[58] R. Zhang, H. Wu, J. Ni, C. Zhao, Y. Chen, C. Zheng, X. Zhang, Guided proliferation and bone-forming functionality on highly ordered large diameter TiO_2 nanotube arrays, Mater. Sci. Eng. C 53 (2015) 272–279, https://doi.org/10.1016/j.msec.2015.04.046.

[59] N. Gui, W. Xu, A.N. Abraham, D.E. Myers, E.L.H. Mayes, K. Xia, R. Shukla, M. Qian, A comparative study of the effect of submicron porous and smooth ultrafine-grained Ti-20Mo surfaces on osteoblast responses, J. Biomed. Mater. Res., Part A 106 (7) (2018) 2020–2033, https://doi.org/10.1002/jbm.a.36402.

[60] E. Huethorst, M.F. Cutiongco, F.A. Campbell, A. Saeed, R. Love, P.M. Reynolds, M. J. Dalby, N. Gadegaard, Customizable, engineered substrates for rapid screening of cellular cues, Biofabrication 12 (2) (2020) 025009, https://doi.org/10.1088/1758-5090/ab5d3f.

[61] Z.K. Cui, S. Kim, J.J. Baljon, M. Doroudgar, M. Lafleur, B.M. Wu, T. Aghaloo, M. Lee, Design and characterization of a therapeutic non-phospholipid liposomal nanocarrier with osteoinductive characteristics to promote bone formation, ACS Nano 11 (8) (2017) 8055–8063, https://doi.org/10.1021/acsnano.7b02702.

[62] J. Zhang, J. Liu, C. Wang, F. Chen, X. Wang, K. Lin, A comparative study of the osteogenic performance between the hierarchical micro/submicro-textured 3D-printed Ti_6Al_4V surface and the SLA surface, Bioact. Mater. 5 (1) (2020) 9–16, https://doi.org/10.1016/j.bioactmat.2019.12.008.

[63] J. Veliscek-Carolan, A. Rawal, V. Luca, T.L. Hanley, Zirconium phosphonate sorbents with tunable structure and function, Microporous Mesoporous Mater. 252 (2017) 90–104, https://doi.org/10.1016/j.micromeso.2017.05.059.

[64] S. Zhang, K. Fang, F. Ye, Q. Zhou, G. Huang, L. Wang, S.-T. Pan, Preparation of zirconium hydrogen phosphate coatings on alkali thermal titanium via a one-step sol-gel method to improve the friction resistance, bioactivity, and osteogenic potential, Appl. Surf. Sci. 682 (2025) 161596, https://doi.org/10.1016/j.apsusc.2024.161596.

[65] K.S. Brammer, S. Oh, C.J. Cobb, L.M. Bjursten, H. van der Heyde, S. Jin, Improved bone-forming functionality on diameter-controlled TiO_2 nanotube surface, Acta Biomater. 5 (8) (2009) 3215–3223, https://doi.org/10.1016/j.actbio.2009.05.008.

[66] W. Huang, S. Yang, J. Shao, Y.-P. Li, Signaling and transcriptional regulation in osteoblast commitment and differentiation, Front. Biosci-Landmrk. 12 (2007) 3068–3092, https://doi.org/10.2741/2296.

[67] H.J. Kim, W.J. Kim, H.M. Ryoo, Post-translational regulations of transcriptional activity of Runx2, Mol. Cells 43 (2) (2020) 160–167, https://doi.org/10.14348/molcells.2019.0247.

[68] C.Y. Wang, Z.X. Qin, Y. Wei, J.X. Hao, Y.F. Zhu, F. Zhao, K. Jiao, H. Ehrlich, F. R. Tay, L.N. Niu, The immunomodulatory effects of RNA-based biomaterials on bone regeneration, Acta Biomater. 162 (2023) 32–43, https://doi.org/10.1016/j.actbio.2023.03.031.

[69] W.R. Wang, J. Li, J.T. Gu, B.W. Hu, W. Qin, Y.N. Zhu, Z.X. Guo, Y.X. Ma, F. Tay, K. Jiao, L. Niu, Optimization of lactoferrin-derived amyloid coating for enhancing soft tissue seal and antibacterial activity of titanium implants, Adv. Healthcare Mater. 12 (11) (2023) e2203086, https://doi.org/10.1002/adhm.202203086.

[70] G. Li, W. Liu, L. Liang, T. Liu, Y. Tian, H. Wu, Preparing Sr-containing nano-structures on micro-structured titanium alloy surface fabricated by additively manufacturing to enhance the anti-inflammation and osteogenesis, Colloids Surf. B Biointerfaces 218 (2022) 112762, https://doi.org/10.1016/j.colsurfb.2022.112762.

[71] Y. Yang, Y. Lin, Z. Zhang, R. Xu, X. Yu, F. Deng, Micro/nano-net guides M2-pattern macrophage cytoskeleton distribution via Src-ROCK signalling for enhanced angiogenesis, Biomater. Sci. 9 (9) (2021) 3334–3347, https://doi.org/10.1039/d1bm00116g.

[72] W.C. Xu, X. Dong, J.L. Ding, J.C. Liu, J.J. Xu, Y.H. Tang, Y.P. Yi, C. Lu, W. Yang, J. S. Yang, Y. Gong, J.L. Zhou, Nanotubular TiO_2 regulates macrophage M2 polarization and increases macrophage secretion of VEGF to accelerate endothelialization via the ERK1/2 and PI3K/AKT pathways, Int. J. Nanomed. 14 (2019) 441–455, https://doi.org/10.2147/IJN.S188439.

[73] J. Luo, Y. He, F. Meng, N. Yan, Y. Zhang, W. Song, The role of autophagy in M2 polarization of macrophages induced by micro/nano topography, Int. J. Nanomed. 15 (2020) 7763–7774, https://doi.org/10.2147/IJN.S270100.

[74] R. Guo, A.R. Merkel, J.A. Sterling, J.M. Davidson, S.A. Guelcher, Substrate modulus of 3D-printed scaffolds regulates the regenerative response in subcutaneous implants through the macrophage phenotype and Wnt signaling, Biomaterials 73 (2015) 85–95, https://doi.org/10.1016/j.biomaterials.2015.09.005.

[75] C. Mao, W. Yu, M. Jin, Y. Wang, X. Shang, L. Lin, X. Zeng, L. Wang, E. Lu, Mechanobiologically optimized Ti-35Nb-2Ta-3Zr improves load transduction and enhances bone remodeling in tilted dental implant therapy, Bioact. Mater. 16 (2022) 15–26, https://doi.org/10.1016/j.bioactmat.2022.03.005.

[76] L.J. Wu, Y.W. Dong, L.T. Yao, C.T. Liu, A.M. Al-Bishari, K.H.R. Yie, H.L. Zhang, J. S. Liu, G. Wu, Nanoporous tantalum coated zirconia implant improves osseointegration, Ceram. Int. 46 (11) (2020) 17437–17448, https://doi.org/10.1016/j.ceramint.2020.04.038.

[77] M.T. Ahmadian, K. Firoozbakhsh, G. Ghanati, The dynamic analysis of a novel dental implant with a viscoelastic internal damping layer. 2010 17th Iranian Conference of Biomedical Engineering (ICBME), 2010, pp. 1–4, https://doi.org/10.1109/icbme.2010.5704999. Isfahan, Iran.